Monthly Notices of the ROYAL ASTRONOMICAL SOCIETY

MNRAS **514,** 5056–5073 (2022) https://doi.org/10.1093/mnras/stac1603
Advance Access publication 2022 June 14

Hot-mode accretion and the physics of thin-disc galaxy formation

Zachary Hafen [1,2★] Jonathan Stern [2,3★] James Bullock [1★] Alexander B. Gurvich [2] Sijie Yu [1] Claude-André Faucher-Giguère [2] Drummond B. Fielding [4] Daniel Anglés-Alcázar,[4,5] Eliot Quataert,[6] Andrew Wetzel [7] Tjitske Starkenburg,[2] Michael Boylan-Kolchin [8] Jorge Moreno [1,9,10,11] Robert Feldmann [12] Kareem El-Badry [13,14] T. K. Chan [15] Cameron Trapp [16] Dušan Kereš[16] and Philip F. Hopkins [11]

[1]*Department of Physics and Astronomy, University of California Irvine, Irvine, CA 92697, USA*
[2]*Department of Physics, Astronomy and CIERA, Northwestern University, 1800 Sherman Ave, Evanston, IL 60201, USA*
[3]*School of Physics, Astronomy, Tel Aviv University, Tel Aviv 69978, Israel*
[4]*Center for Computational Astrophysics, Flatiron Institute, 162 5th Ave, New York, NY 10010, USA*
[5]*Department of Physics, University of Connecticut, 196 Auditorium Road, U-3046, Storrs, CT 06269-3046, USA*
[6]*Department of Astrophysical Sciences, Princeton University, Princeton, NJ 08544, USA*
[7]*Department of Physics, Astronomy, University of California, Davis, CA-95616, USA*
[8]*Department of Astronomy, The University of Texas at Austin, 2515 Speedway, Stop C1400, Austin, TX 78712-1205, USA*
[9]*Downing College, University of Cambridge, Cambridge CB3 OHA, UK*
[10]*Department of Physics and Astronomy, Pomona College, Claremont, CA 91711, USA*
[11]*TAPIR, Mailcode 350-17, California Institute of Technology, Pasadena, CA 91125, USA*
[12]*Institute for Computational Science, University of Zurich, Zurich CH-8057, Switzerland*
[13]*Center for Astrophysics | Harvard, Smithsonian, 60 Garden Street, Cambridge, MA 02138, USA*
[14]*Harvard Society of Fellows, 78 Mount Auburn Street, Cambridge, MA 02138, USA*
[15]*Institute for Computational Cosmology, Department of Physics, Durham University, South Road, Durham DH1 3LE, UK*
[16]*Department of Physics, Center for Astrophysics and Space Sciences, University of California, San Diego, 9500 Gilman Drive, La Jolla, CA 9209, USA*

Accepted 2022 June 8. Received 2022 June 6; in original form 2022 January 19

ABSTRACT

We use FIRE simulations to study disc formation in $z \sim 0$, Milky Way-mass galaxies, and conclude that a key ingredient for the formation of thin stellar discs is the ability for accreting gas to develop an aligned angular momentum distribution via internal cancellation prior to joining the galaxy. Among galaxies with a high fraction (> 70 per cent) of their young stars in a thin disc ($h/R \sim 0.1$), we find that: (i) hot, virial-temperature gas dominates the inflowing gas mass on halo scales ($\gtrsim$20 kpc), with radiative losses offset by compression heating; (ii) this hot accretion proceeds until angular momentum support slows inward motion, at which point the gas cools to $\lesssim 10^4$ K; (iii) prior to cooling, the accreting gas develops an angular momentum distribution that is aligned with the galaxy disc, and while cooling transitions from a quasi-spherical spatial configuration to a more-flattened, disc-like configuration. We show that the existence of this 'rotating cooling flow' accretion mode is strongly correlated with the fraction of stars forming in a thin disc, using a sample of 17 $z \sim 0$ galaxies spanning a halo mass range of $10^{10.5}$ M$_\odot \lesssim M_{\rm h} \lesssim 10^{12}$ M$_\odot$ and stellar mass range of 10^8 M$_\odot \lesssim M_\star \lesssim 10^{11}$ M$_\odot$. Notably, galaxies with a thick disc or irregular morphology do not undergo significant angular momentum alignment of gas prior to accretion and show no correspondence between halo gas cooling and flattening. Our results suggest that rotating cooling flows (or, more generally, rotating subsonic flows) that become coherent and angular momentum-supported prior to accretion on to the galaxy are likely a necessary condition for the formation of thin, star-forming disc galaxies in a ΛCDM universe.

Key words: galaxies: evolution – galaxies: haloes – cosmology: theory.

1 INTRODUCTION

Our present picture for the formation of galactic discs can be largely traced to analytic ideas first explored by Fall & Efstathiou (1980), where a galaxy's angular momentum is intimately tied to the corresponding properties of its host dark matter halo. Collapsing structures in an otherwise expanding universe will be spun up by the large-scale matter field (Peebles 1969); this can deliver enough angular momentum to allow (at least some) galaxies to have significant angular-momentum support (e.g. Mo, Mao & White 1998). While these ideas have provided foundational insights into the origin of disc galaxies in a ΛCDM universe, our understanding of disc formation, and thin-disc galaxy formation in particular, remains incomplete. While dark matter haloes of all masses are predicted to have similar angular momentum distributions (e.g. Barnes & Efstathiou 1987), disc fraction varies noticeably as a function of

★ E-mail: zachary.h.hafen@gmail.com (ZH); sternjon@tauex.tau.ac.il (JS); bullock@uci.edu (JB)

galaxy mass (e.g. Bernardi et al. 2010; Bluck et al. 2014; Moffett et al. 2016). Moreover, dark matter spin alone is insufficient to explain the detailed properties of discs formed in cosmological simulations (e.g. Sales et al. 2012; Garrison-Kimmel et al. 2018a; Rohr et al. 2021).

Given what we know about the angular momentum distribution in galactic haloes, it is somewhat surprising that so many galaxies are dominated by *thin* discs, with scale heights and vertical velocity dispersions that are small compared to their scale radii and circular speeds, $h/R \sim \sigma_z/V_c \sim 0.1$ (Kregel, Van Der Kruit & De Grijs 2002). We know, for example, that the angular momentum distribution of dark matter (Bullock et al. 2001; Lian et al. 2018) and gas (Stewart et al. 2013; DeFelippis et al. 2020) in galactic haloes is quite *broad*. This means that in order for a tightly ordered thin disc to emerge, the gas must become coherently aligned along a single plane *after* being part of the quasi-spherical extended galactic halo and *before* forming stars. This suggests that the process by which gas is deposited from the galactic halo into the galaxy, and how this process affects the angular momentum distribution, is an essential aspect of thin-disc formation.

The process by which gas is deposited into a galaxy from the circumgalactic medium (CGM) has been explored considerably (e.g. Kereš et al. 2005, 2009a; Dekel & Birnboim 2006; Faucher-Giguère, Kereš & Ma 2011; van de Voort et al. 2011; Anglés-Alcázar et al. 2017; Stevens et al. 2017; Martin et al. 2019). Broadly speaking, two paths of galaxy fueling have been identified: hot mode and cold mode. In the cold-mode case, gas is deposited into the galaxy without ever virializing; this occurs typically in lower-mass haloes, where the gas cooling time is shorter than the infall time. In hot-mode accretion, which dominates for massive haloes at late times ($M_{\rm vir} \gtrsim 10^{12}\,\dot{M}$, $z \lesssim 1$; e.g. Faucher-Giguère et al. 2011; Van de Voort et al. 2011; Joung et al. 2012; Murante et al. 2012; Van de Voort & Schaye 2012; Nelson et al. 2013; Fielding et al. 2017), gas first shock-heats to the halo virial temperature, and then radiates away its gravitational and thermal energy prior to accreting on to the galaxy. Our own Milky Way (MW) is one such galaxy for which hot-mode accretion is expected to dominate. As discussed above, we expect the mode of gas delivery, and the precise means by which gas mixes, cools, and accretes to have a substantial bearing on the ability to form thin, coherently rotating discs.

In cold mode accretion, cool ($T \sim 10^4$ K) gas travels from cosmological scales through the CGM and intergalactic medium, and into the galaxy in filaments (e.g. Kereš et al. 2005, 2009b; Dekel & Birnboim 2006; Faucher-Giguère et al. 2011; Martin et al. 2019), often along with embedded satellite galaxies (e.g. Faucher-Giguère et al. 2015, 2016; Hafen et al. 2019; Esmerian et al. 2021). This mode is expected to dominate the mass inflow rate at high redshifts ($z \gtrsim 2$; e.g. Dekel et al. 2009; Kereš et al. 2009a; Huscher et al. 2021). It is unclear, however, if the cool filaments remain intact down to the galaxy, or rather heat up and dissolve into the surrounding hot phase (e.g. Kereš & Hernquist 2009; Nelson et al. 2016; Mandelker et al. 2016, 2018, 2020), in which case hot accretion on to the galaxy would also be important at high redshift). Cool filamentary inflow typically carries more specific angular momentum (on average) than either hot gas or dark matter (e.g. Stewart et al. 2017), and systems fed by cold accretion often have extended, messy, 'cold flow discs' orbiting the galaxy (e.g. Stewart et al. 2011, 2013; Danovich et al. 2015; Dekel, Lapiner & Dubois 2019). However, the tendency for such gas to have a wide range of trajectories as it approaches the galactic region may hinder the ability to develop a thin, coherently aligned structure prior to star formation. Also, the fact that thin-disc galaxies are common only among fairly massive systems ($L \sim 0.1L_\star - L_\star$) at lower redshift (e.g. Kranz, Slyz & Rix 2003; Kassin, de Jong & Weiner 2006; Kassin et al. 2012b; Simons et al. 2015, 2017; Bizyaev et al. 2021), suggests that cold-mode delivery may not be conducive to thin-disc formation.

An alternative possibility is that hot-mode accretion, believed to dominate in more massive haloes at lower redshift, is more favourable to thin-disc formation. Indeed, some cosmological simulations show a correlation between hot accretion and disc formation, albeit with wide scatter (Sales et al. 2012). The connection depends on the specific mechanics of this accretion mode, and on whether the hot gas manages to cool and accrete rather than being reheated by galactic feedback processes. One possible subset of hot-mode accretion is instability-driven accretion, wherein gas precipitates out of a hydrostatic hot halo due to thermal instabilities, forming cool clouds that lose buoyancy and accrete on to the galaxy (e.g. Fall & Rees 1985; Maller & Bullock 2004; McCourt et al. 2012; Voit et al. 2015; Armillotta, Fraternali & Marinacci 2016; Gronke & Oh 2020; Fielding et al. 2020; Voit 2021). Alternatively, radiative cooling in the hot CGM can cause the entire hot halo to flow radially inward. In this latter scenario, compression heating of the hot gas due to the inflow roughly balances radiative losses, so the hot gas stays at an approximately constant temperature. This type of hot accretion has been termed a 'cooling flow' in the context of galaxy cluster studies (Mathews & Bregman 1978; Cowie, Fabian & Nulsen 1980; Fabian, Nulsen & Canizares 1984; Balbus 1988; Bertschinger 1989; McNamara & Nulsen 2007), and was recently revisited in the context of galaxy-scale haloes by Stern et al. (2019). A hot inflow is qualitatively distinct from precipitation, since the entire hot medium inflows on a cooling time-scale, which implies that thermal instabilities do not have time to grow substantially (Balbus & Soker 1989, see also fig. 10 of Stern et al. 2019). The angular momentum content of such hot inflows was considered by Stern et al. (2020), who showed that angular momentum sets a maximum accretion rate in which the inflow remains hot and subsonic down to the galaxy scale. In the present paper, we demonstrate that such cooling flows with angular momentum (i.e. 'rotating cooling flows') are the primary mode of gas accretion on to discy MW-mass galaxies at $z \sim 0$ in the Feedback in Realistic Environment (FIRE)-2 cosmological simulations (Hopkins et al. 2018), and may be a necessary condition for the formation of thin star-forming discs.

The analysis here follows Stern et al. (2021b), which showed that the formation of discs is closely connected to the formation of a virialized and stable hot CGM. Yu et al. (2021) subsequently showed that the emergence of an inner virialized CGM correlates specifically with a transition from *thick*-disc to *thin*-disc formation. The conditions necessary for thin-disc formation thus appear to correlate with the conditions necessary for the onset of hot accretion modes, and cooling flows in particular. In contrast, it seems unlikely that the transition to a thin disc in FIRE-2 is driven by increased ejection of low angular momentum gas by feedback as suggested by analysis of other simulations (e.g. Brook et al. 2011; Übler et al. 2014; Genel et al. 2015; DeFelippis et al. 2017), since in FIRE-2 the mass loss due to feedback drops when the galaxy becomes discy (Hafen et al. 2020; Pandya et al. 2021; Stern et al. 2021a). These findings motivate the exploration that follows.

Central to our analysis, and the analyses of Stern et al. and Yu et al., are the FIRE simulations (Hopkins et al. 2014, 2018)[1] a set of 'zoom-in' simulations that resolve stellar feedback on the scale of giant molecular clouds in the interstellar medium (ISM; Benincasa et al. 2020; Guszejnov et al. 2020), producing winds that

[1] https://fire.northwestern.edu/

Table 1. Simulation parameters.

Name	$f_{\rm thin\,disk,\,recent}$	$M_{\rm vir}$ $\rm M_\odot$	$M_\star$ $\rm M_\odot$	$R_{\rm vir}$ kpc	$\Delta f_{\rm aligned}$	Metal diffusion?	Reference
m12i	0.94	1.1×10^{12}	7.3×10^{10}	268	0.34	✓	Wetzel et al. (2016)
m12i_core	0.89	1.1×10^{12}	8.0×10^{10}	274	0.34		Hopkins et al. (2018)
m12b	0.88	1.3×10^{12}	1.0×10^{11}	286	0.35	✓	Garrison-Kimmel et al. (2019)
m12c	0.87	1.3×10^{12}	6.8×10^{10}	283	0.25	✓	Garrison-Kimmel et al. (2019)
m12f	0.87	1.5×10^{12}	9.7×10^{10}	302	0.24	✓	Garrison-Kimmel et al. (2017)
m11h	0.52	1.8×10^{11}	3.9×10^{9}	146	0.047	✓	El-Badry et al. (2018a)
m12w	0.49	9.5×10^{11}	6.5×10^{10}	253	0.15	✓	Samuel et al. (2020)
m12m	*0.46	1.5×10^{12}	1.4×10^{11}	298	0.26		Hopkins et al. (2018)
m11b	0.44	4.4×10^{10}	1.2×10^{8}	92.4	0.12		Chan et al. (2018)
m12r	0.31	1.0×10^{12}	2.4×10^{10}	257	0.11	✓	Samuel et al. (2020)
m12z	0.11	8.0×10^{11}	2.5×10^{10}	242	0.052	✓	Garrison-Kimmel et al. (2019)
m11i	0.046	7.0×10^{10}	1.0×10^{9}	106	0.013	✓	El-Badry et al. (2018a)
m11c	0.035	1.4×10^{11}	9.5×10^{8}	137	0.0068		Hopkins et al. (2018)
m11e	0.031	1.5×10^{11}	1.6×10^{9}	136	0.044	✓	El-Badry et al. (2018a)
m11d	0.03	2.9×10^{11}	4.9×10^{9}	169	0.0026	✓	El-Badry et al. (2018a)
m11a	0.022	4.1×10^{10}	1.3×10^{8}	90.3	−0.022		Chan et al. (2018)
m11q	0.0066	1.5×10^{11}	7.4×10^{8}	138	0.0045	✓	Hopkins et al. (2018)

Properties at $z = 0$ of the sample of FIRE galaxies analysed in this work. The value of $f_{\rm thin\,disk,\,recent}$ is the fraction of stars formed in the last Gyr prior to $z = 0$ that are in a thin-disc configuration ($j/j_c(E) > 0.8$; e.g. Yu et al. 2021). The m12m galaxy has a sizable bar, which drives the thin-disc fraction lower by our adopted definition (marked by *). The value of $\Delta f_{\rm aligned}$ is a measure of the relation between cooling and flattening in accreted gas (Section 3.3). The 'metal diffusion' column marks whether or not the simulation includes a subgrid prescription for metal diffusion.

expand into the CGM and interact with accreting gas (Muratov et al. 2015, 2017; Anglés-Alcázar et al. 2017; Hafen et al. 2019, 2020; Pandya et al. 2021). The resultant galaxies are broadly consistent with the stellar mass–halo mass relation (Hopkins 2017), satellite galaxy populations (Wetzel et al. 2016; Garrison-Kimmel et al. 2019; Samuel et al. 2020), and can have thin-discs consistent with MW-like galaxies (Ma et al. 2017; Garrison-Kimmel et al. 2018b; El-Badry et al. 2018b; Yu et al. 2021), albeit potentially with hotter kinematics (Sanderson et al. 2020). Here, we use the FIRE-2 simulations to study gas accretion on to $z \sim 0$ galaxies and its relation to thin-disc morphology. Our approach uses the particle-tracking methodology developed in Hafen et al. (2019, 2020) to explore the mechanics of rotating cooling flows near the disc–halo interface where angular momentum support is substantial. Our analysis goes beyond 1D steady-state solutions for rotating cooling flows developed in classic ICM studies (e.g. Cowie et al. 1980), and extends the idealized 3D simulations of rotating cooling flows in Stern et al. (2020) to a more realistic cosmological setting. Our work is complementary to Trapp et al. (2021), who characterized the phenomenological properties of accretion on to MW-like FIRE galaxies, and the particle tracking analysis of Anglés-Alcázar et al. (2017), who provided an overview of the connection between the cosmic baryon cycle and galaxy mass assembly.

This paper is structured as follows. In Section 2, we describe our sample of FIRE simulations and the sample of accreting particles selected from the simulations. In Section 3, we analyse the characteristics and mechanics of gas accretion on to $z \sim 0$ galaxies in FIRE, and their relation to thin-disc morphology in the central galaxy. We discuss our results in Section 4 and conclude in Section 5.

2 METHODS

2.1 Simulations

We analyse hydrodynamical cosmological zoom-in simulations produced as part of the FIRE project (Hopkins et al. 2014). The simulation sample, listed in Table 1, were run with the FIRE-2 version (Hopkins et al. 2018) of the gravity and hydrodynamics code GIZMO[2] (Hopkins 2015). The simulations were produced using the meshless finite-mass mode of GIZMO, a Lagrangian method with no inter-element mass flux. This enables us to track the history of each resolution element. The full details of simulations produced with the FIRE-2 code are available in Hopkins et al. (2018). The FIRE simulations include detailed prescriptions for star formation and stellar feedback. Each star particle contributes to the simulation momentum from radiation pressure; energy, momentum, mass, and metals from Type Ia and II supernovae and stellar winds; and photo-ionization and photo-electric heating. The mass of the resolution elements ranges from 2100 to 7100 $\rm M_\odot$. Star formation is limited to self-gravitating, self-shielding (molecular) gas with a density of at least $n_{\rm SF} = 1000\,\rm cm^{-3}$. In addition to stellar radiation, the simulations include a uniform meta-galactic radiation background that ionizes gas in the intergalactic and CGM (Faucher-Giguère et al. 2009). In the simulations and throughout our analysis, we use a standard flat ΛCDM cosmology with $\Omega_{\rm m} \approx 0.32$, $\Omega_\Lambda = 1 - \Omega_{\rm m}$, $\Omega_{\rm b} \approx 0.049$, and $H_0 \approx 67\,\rm km\,s^{-1}\,Mpc^{-1}$ (e.g. Planck Collaboration 2018).

Fig. 1 shows edge-on mock Hubble images for the $z = 0$ snapshots of four of our simulated galaxies, neglecting dust attenuation to more clearly illustrate the stellar distribution. The bottom-left and top panels show three MW-mass galaxies (m12i, m12b, and m12c) while the bottom-right panel shows a $M_\star \sim 5 \times 10^9$ $\rm M_\odot$ dwarf galaxy, m11d. As noted in previous studies (El-Badry et al. 2018b; Garrison-Kimmel et al. 2018b), MW-mass galaxies in FIRE typically have thin-disc morphologies, while lower mass galaxies show a thick disc/irregular morphology. We quantify this trend using $f_{\rm thin\,disc,\,recent}$, defined as the mass fraction of stars with age <1 Gyr (at $z = 0$) that have $j_z/j_c(E) > 0.8$. Here j_z is the specific angular momentum in the z direction and $j_c(E)$ is the angular momentum that the star would have if it had the same energy but was in a circular orbit. The z-axis is defined as the direction of the total angular momentum vector of stars inside the galaxy. This definition of the thin disc is

[2] http://www.tapir.caltech.edu/~phopkins/Site/GIZMO.html

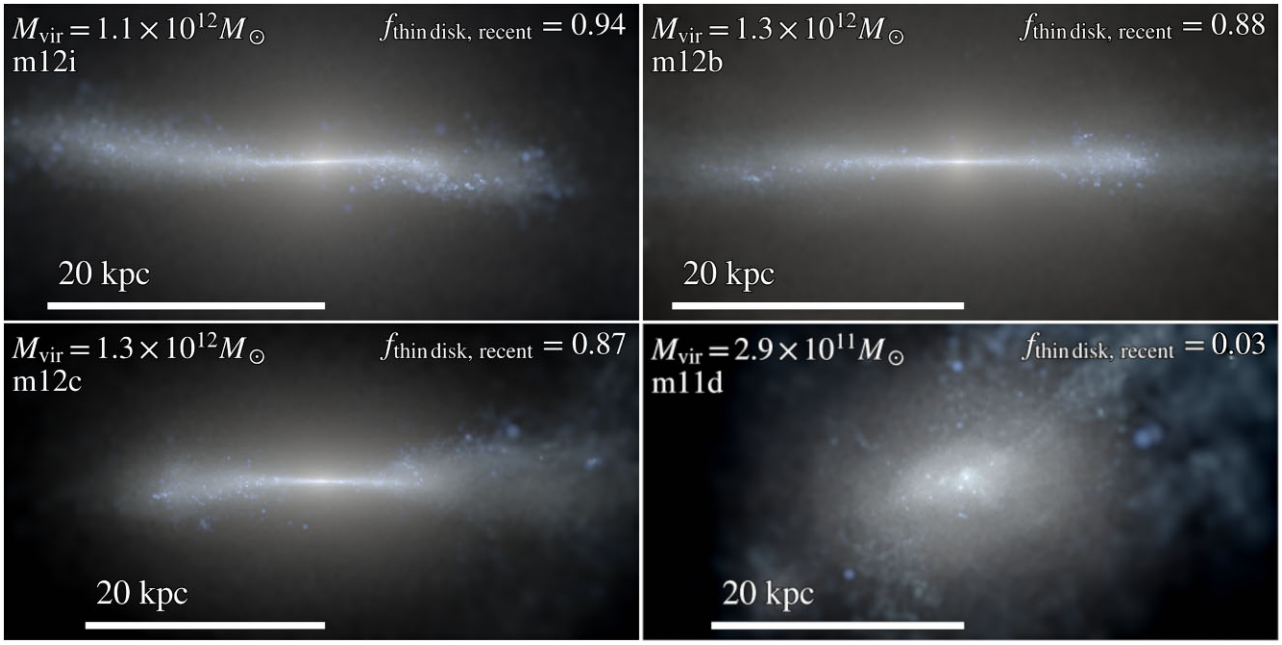

Figure 1. Mock Hubble images of four $z = 0$ galaxies in the FIRE-2 simulations. Halo masses are noted in the panels, together with the mass fraction of young (<1 Gyr) stars that reside in a thin disc. The MW-mass galaxies have thin disc morphologies (bottom-left, top), while the lower mass galaxy has an irregular morphology (bottom-right).

the same definition used in Yu et al. (2021). Values of $j_z/j_c(E) > 0.8$ correspond to height to size ratios $h/R \sim 0.1$ (confirmed across a number of choices of h and R) and rotation to dispersion ratios $V_{\rm rot}/\sigma_z \sim 10$, and correlate strongly with the observed thin-disc fraction in the r band (Appendix A). The values of $f_{\rm thin\,disc,\,recent}$ are noted in Fig. 1 and listed in Table 1. Throughout we will refer to galaxies with $f_{\rm thin\,disc,\,recent} > 0.6$ as thin-disc galaxies and galaxies with $f_{\rm thin\,disc,\,recent} < 0.6$ as irregular or thick-disc galaxies.

2.2 Analysis

For each galaxy, we use the particle tracking method described in Hafen et al. (2019, 2020), which in turn applies insight from previous particle-tracking applied to the FIRE simulations (Anglés-Alcázar et al. 2017). We select an unbiased sample of resolution elements (particles) that have accreted on to the central galaxy during the last Gyr prior to $z = 0$. To select such particles, we require that they are (1) within the galaxy radius $r_{\rm gal}$ at $z = 0$, either in stars or in gas with density $n_{\rm H} > 0.13$ cm^{-3}, and (2) within the CGM (gas at $0.1 - 1 r_{\rm vir}$) in the snapshot corresponding to 1 Gyr prior to $z = 0$. Throughout the paper, we use r for the 3D distance. We define $r_{\rm gal} = 4 r_{\star,\,0.5}$, following Hafen et al. (2019, 2020), where $r_{\star,\,0.5}$ is the stellar half-mass radius. When selected this way, the number of particles that meet these conditions ranges from ∼1000 for the low-mass irregular galaxies to ∼10^5 for the thin-disc galaxies. For each selected particle, we retrieve the full history of the particle, including temperature, density, and metallicity. We discard a small fraction (< 2 per cent) of the particles whose mass increases by a factor of 2 as a consequence of mass deposition by stellar feedback.[3] In Appendix B, we show that the accretion histories of selected particles are representative of the accretion histories of all stars formed within 1 Gyr of $z = 0$, and that around thin-disc galaxies our selected particles are drawn from the angular momentum distribution of the CGM without bias.

A key time for our analysis is the accretion time $t_{\rm acc}$, the time at which a particle first accretes on to the galaxy after being identified as part of the CGM 1 Gyr prior to $z = 0$. Explicitly, $t_{\rm acc}$ is:

$$t_{\rm acc} \equiv t(\text{last snapshot outside galaxy}), \quad (1)$$

i.e. the last snapshot prior to the particle matching the above criteria for being within a galaxy.

Another key time for our analysis is the last time a particle cools prior to entering the galaxy. For a given particle, we define this time as:

$$t_{10^5\,\rm K} \equiv t(\text{last snapshot outside galaxy with } T > 10^5\,\text{K}), \quad (2)$$

i.e. the last snapshot the particle was hot prior to $t_{\rm acc}$. For gas that cools as it accretes, $t_{10^5\,\rm K}$ occurs as the gas passes through the galaxy–halo interface. In all haloes, we find that $\gtrsim 99$ per cent of tracked particles heat above $T > 10^5$ K at some point prior to accretion, even in our low-mass haloes where the virial temperature is $T \approx 2 \times 10^5$ K and accretion on to the galaxy is dominated by cold inflows. In such haloes, heating is typically temporary due to the short cooling times, but hot gas still comprises $\gtrsim 30$ per cent of the halo's gas mass at any given time (Hafen et al. 2019, 2020). Below we analyse the statistical properties of all accreting particles as a function of time relative to their cooling time ($t - t_{10^5\,\rm K}$) or relative to their accretion time ($t - t_{\rm acc}$).

3 RESULTS

To characterize gas accretion, we analyse the central galaxy and its CGM from $z = 0$ to 1 Gyr prior. Fig. 2 shows a visual overview of how gas accretes on to `m12i` – a MW-mass galaxy that forms a substantial thin disc ($f_{\rm thin\,disk,\,recent} = 0.94$). The top and right-hand panels plot the temperature and spatial evolution of accreting gas

[3]These particles pose a problem for our tracking method because the history of the additional mass is not recorded, and because they are split into multiple particles after gaining sufficient mass.

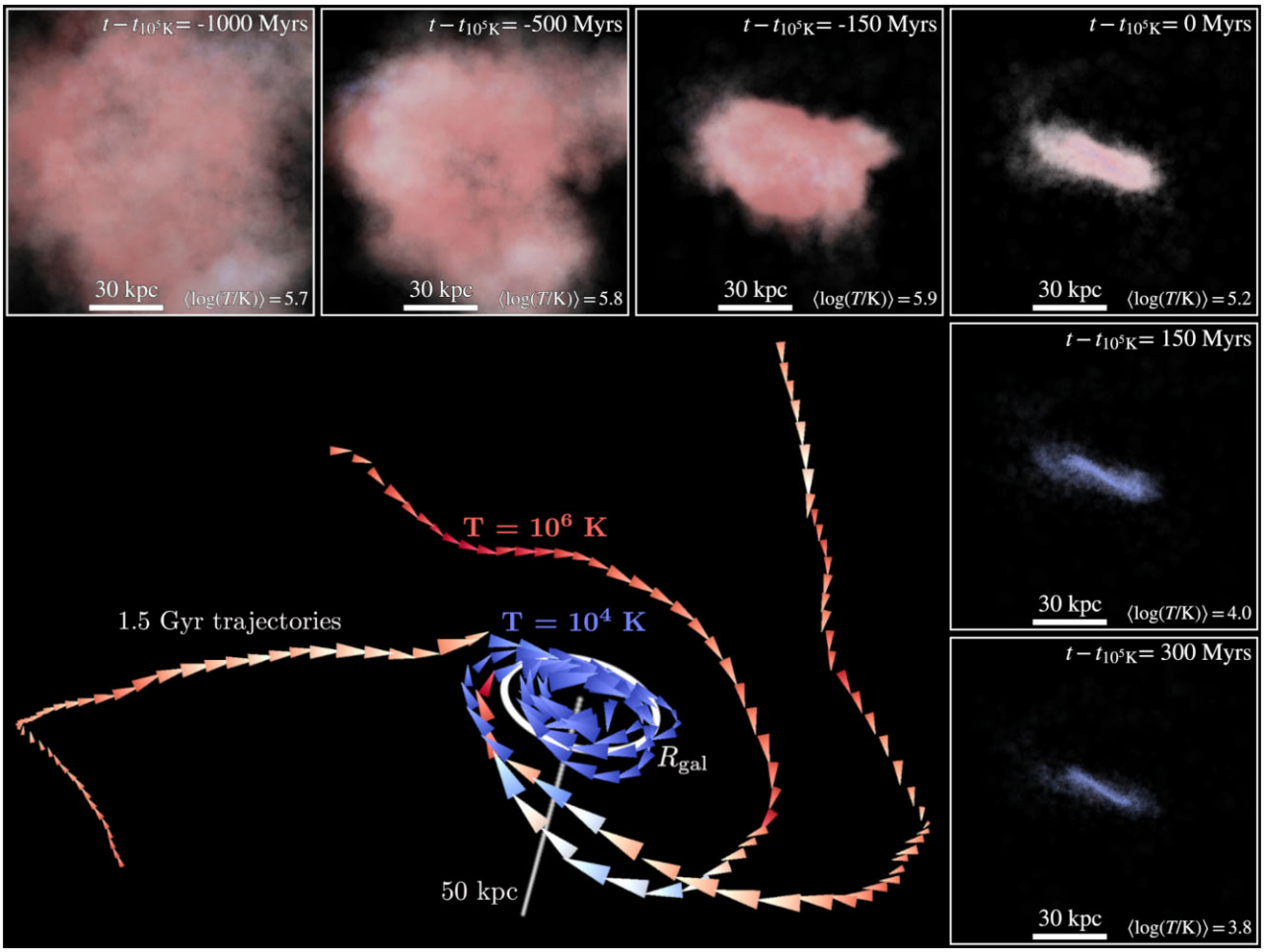

Figure 2. Gas accretion on to a MW-mass disc galaxy in FIRE, `m12i`, near $z \approx 0$. **Top and right-hand panels:** temperature and spatial evolution of accreting gas with respect to $t_{10^5\,\mathrm{K}}$, defined as the last time at which the gas cools below 10^5 K prior to accreting on to the galaxy. Red, white, and blue indicates $T = 10^6$ 10^5, and 10^4 K, respectively. **Bottom-left panel:** three representative trajectories for accreting gas elements. The panels show that accretion is hot ($\approx 10^6$ K) and contracts quasi-spherically at early times relative to the time of cooling. At the time of cooling, the geometry of accreting gas transitions from a quasi-spherical distribution at $t - t_{10^5\,\mathrm{K}} < -150$ Myr to a cool disc at $t - t_{10^5\,\mathrm{K}} > 150$ Myr.

versus time prior to cooling ($t - t_{10^5\,\mathrm{K}}$), while the bottom-left panel plots three representative trajectories for accreting gas elements. The trajectories were visualized using the FIREFLY visualization software (Geller & Gurvich 2018).[4] The trajectory colour scales with temperature, with red, white, and blue, indicating $T = 10^6$, 10^5, and 10^4 K, respectively. The figure shows that at early times relative to cooling ($t - t_{10^5\,\mathrm{K}} \sim -1000$ Myr) the accretion is hot ($\approx 10^6$ K) and contracts quasi-spherically. Then, around the time of cooling the geometry of accreting gas transitions from quasi-spherical at $t - t_{10^5\,\mathrm{K}} = -150$ Myr to a cool disc aligned with the galaxy at $t - t_{10^5\,\mathrm{K}} = +150$ Myr. A quantitative analysis of this transition follows in Sections 3.1–3.4.

3.1 Gas inflow on to thin-disc MW analogs is hot through the CGM

Fig. 3 plots various characteristics of accreting gas on the `m12i` thin-disc galaxy, as a function of time relative to the accretion's last cooling time ($t - t_{10^5\,\mathrm{K}}$). In each panel, solid lines and shaded regions mark the medians and 16th–84th percentile ranges of all particles accreted within 0.5–1 Gyr prior to $z = 0$. The lower limit on the time range applied in this figure is to ensure that particles are present for most of the time displayed after $t_{10^5\,\mathrm{K}}$, although removing the limit does not change the qualitative results. In the temperature panel (A), we exclude from the distribution particles that have been converted into stars.

Panel (A) demonstrates that during the 500 Myr prior to cooling for a final time, the inflow is predominantly hot ($\gtrsim 10^5$ K), with a median temperature of 4–8 $\times$ 10^5 K, similar to the halo virial temperature of $T_{\mathrm{vir}}(z = 0) = 6.5 \times 10^5$ K. This is not true by construction – gas could maintain a temperature $T > 10^5$ K for only a short time prior to cooling. In Appendix C (online), we verify that the inflow is predominantly hot also in terms of mass inflow rate. During the time prior to cooling the accreting gas is inflowing towards the galaxy (panel B), from a median $r \approx 55$ kpc at $t - t_{10^5\,\mathrm{K}} = -500$ Myr, to a median $r \approx 18$ kpc $\approx 1.4 r_{\mathrm{gal}}$ at $t = t_{10^5\,\mathrm{K}}$, after which time the inflow decelerates. The characteristic inflow velocity of $v_r \approx -70$ km s^{-1} (panel C) is substantially lower than the circular velocity of 170–200 km s^{-1}. This radial velocity is also smaller than the median sound speed of 100–130 km s^{-1}, indicating a subsonic flow.

[4] A 3D version of these trajectories is available online at zhafen.github.io/rotating-cooling-flows. The FIREFLY homepage is at alexbgurvi.ch/Firefly.

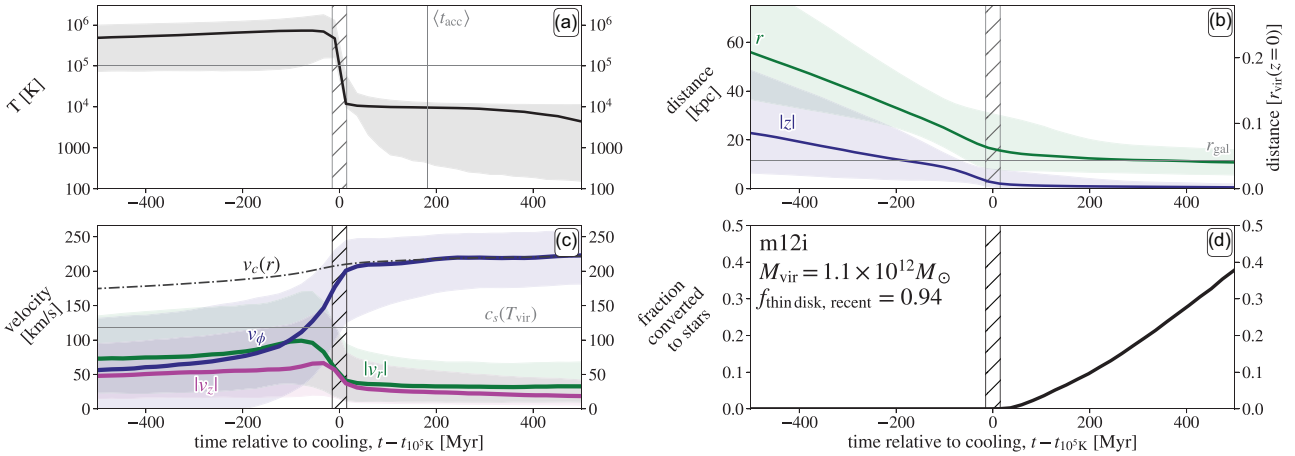

Figure 3. Properties of gas accretion on to a $z \sim 0$ thin-disc galaxy in FIRE (`m12i`), versus time relative to the final cooling time ($t - t_{10^5\,K}$). In each panel, solid lines and shaded regions mark the medians and 16th–84th percentile ranges of all particles accreted within 1 Gyr prior to $z = 0$. (a) Temperature. The inflow is predominantly hot ($\gtrsim 10^5$ K) prior to cooling, with a median temperature approaching $T_{vir} \sim 10^6$ K. At $t = t_{10^5\,K}$ the gas cools (by definition), and achieves temperatures $T \lesssim 10^4$ K or forms stars. (b) 3D distance from halo centre (green) and absolute height from the disc plane (blue). Cooling occurs at $r = 10-30$ kpc, corresponding to $0.7 - 2.5\,r_{gal}$. Prior to cooling, the gas forms an inflow while after cooling the inflow decreases speed. Most of the gas collapses into a disc upon cooling, with a median $|z| \approx 2$ kpc at $t = t_{10^5\,K}$. (c) Velocity components of accretion (coloured lines and bands), relative to the median circular velocity (dash–dotted line). The gas reaches full rotational support upon cooling. The grey line marks the sound speed of virial temperature gas. (d) Fraction of gas converted into stars. Star formation starts after cooling, at a rate of ~ 10 per cent per 100 Myr.

We show below that a similar hot inflow is seen in other thin-disc galaxies in our sample, and that the accretion occurs on a cooling time-scale. Thus, accretion from the CGM on to $z = 0$ thin discs in FIRE is dominated by the inflow of hot, virial temperature gas, as in classic cooling flow solutions (e.g. Fabian et al. 1984). This hot accretion mode, in which the entire hot phase inflows, is qualitatively different from 'precipitation', in which gas clumps cool out of the hot phase at halo scales, lose buoyancy, and subsequently accrete (see introduction). The dominance of a hot inflow over precipitation in MW-like galaxies simulated in FIRE has previously been noted by Esmerian et al. (2021).

3.2 Accretion cools and decelerates at the galaxy–halo interface

Panel (A) in Fig. 3 demonstrates that at $t = t_{10^5\,K}$ the temperature drops quickly from $\sim 10^6$ to $\sim 10^4$ K. Panel (B) shows that this cooling occurs at the galaxy edge or shortly beyond, at $r(t_{10^5\,K}) \approx 10 - 30$ kpc, equivalent to ≈ 0.7–$2.5 r_{gal}$.[5] Less than 10 per cent of particles cool beyond ~ 40 kpc. After cooling to $T \sim 10^4$ K, the temperature further drops to cool ISM temperatures of $100 - 10^4$ K and stars begin to form at a rate of ≈ 10 per cent per 100 Myr (panel D), roughly equal to the average rate in the galaxy ISM. The vertical grey line in panel (A) marks the median time at which the gas accretes, though $t_{acc} - t_{10^5\,K}$ spans ~ 0–500 Myr depending on the particle.

Panel (C) in Fig. 3 demonstrates that cooling at the galaxy scale is further associated with a change in kinematics. The radial inflow velocity $|v_r|$ starts decelerating ≈ 40 Myr prior to cooling, finishing at $v_r \lesssim 50$ km s^{-1} after cooling. The deceleration is associated with v_ϕ reaching v_c, where ϕ is defined with respect to the total angular momentum of stars in the galaxy at $z = 0$, indicating a transition from pressure-support in the hot CGM to rotational-support in the cool ISM. Note that deceleration prior to accretion is possible due to the subsonic nature of the radial hot flow – the gas pressure can adjust close to the galaxy so the transition to a rotating disc happens smoothly rather than in a single shock. Similar results are seen for accretion on to other thin-disc galaxies in our sample (see below), indicating that the majority of accretion on to $z \sim 0$ thin-disc galaxies in FIRE is a hot inflow which cools and decelerates just outside the galaxy. As shown below (Section 3.5; Appendix D (online)), this is *not* the case for galaxies that lack thin discs in our sample. Galaxies that are dominated by thick/irregular morphology demonstrate no such deceleration at the galaxy–halo interface.

[5]Gas can have $r(t_{10^5\,K}) < r_{gal}$ if it is under-dense relative to the galaxy when it crosses r_{gal} ($n_H < 0.13$ cm^{-3}; see Section 2.2).

3.3 Cooling of accreted gas is concurrent with flattening

Panel (B) in Fig. 3 also plots the distance $|z|$ above or below the disc plane as a function of time. The panel shows that as the gas collapses, it becomes increasingly flattened in the disc plane. At the time of cooling, the gas has a median height of ≈ 2 kpc, indicating a disc geometry with height to radius ratio of $|z|/r_{gal} \approx 0.2$, consistent with the transition to rotation support indicated by panel (C). Panel (D) in Fig. 3 emphasizes that all of the star formation occurs after rotation support is achieved and the disc geometry is in place.

This correspondence between a transition to disc geometry and cooling is further explored in Fig. 4, which plots the geometry of accreting gas at different times relative to $t_{10^5\,K}$ for the four galaxies shown in Fig. 1. Times prior to cooling are coloured in red, while times after cooling are plotted in blue. All particles with $t - t_{10^5\,K}$ within ± 30 Myr of the value noted in the legend are included in the distribution. The curves show the PDF of $\cos\theta = z/r$, i.e. θ is the angle between the gas element position and the total angular momentum vector of stars in the galaxy at $z = 0$. A spherical distribution of accreted gas would have a flat PDF with a value of 0.5, while the PDF of an infinitely thin disc would be a δ-function centred at $z/r = 0$. The figure shows that gas accreting on to the three thin-disc galaxies transitions from being distributed quasi-spherically at $t = t_{10^5\,K} - 200$ Myr to being distributed in the galaxy plane at $t = t_{10^5\,K} + 200$ Myr. This indicates that the cooling and flattening of the accreting gas occurs simultaneously in these galaxies, consistent

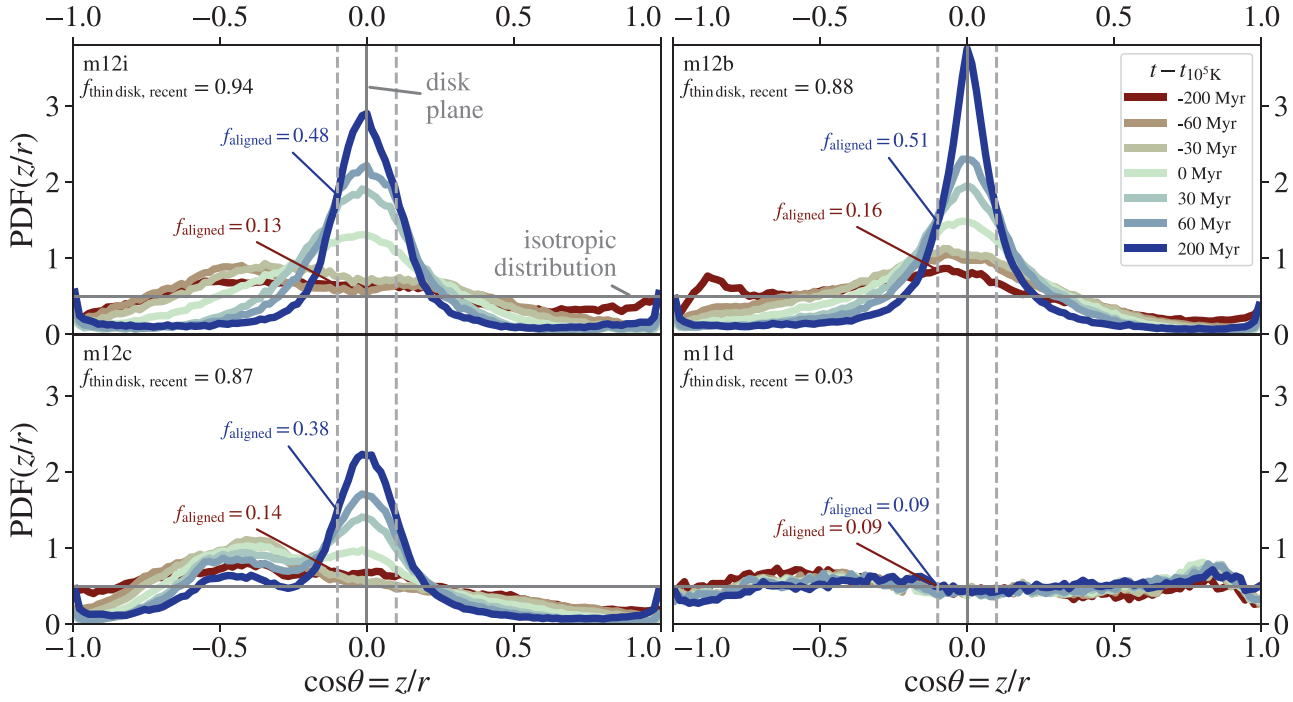

Figure 4. Geometry (ratio of height to radius) of accreting gas, as a function of time relative to the last cooling time. The galaxies displayed are the same as in Fig. 1. In thin-disc galaxies (top and bottom-left panels), the geometry of accreting gas evolves significantly around the time of cooling, from a quasi-spherical distribution prior to cooling (red curves) to a disc-like configuration after cooling (blue curves). In contrast, in the irregular galaxy (bottom-right), accreting gas is roughly spherical both prior to and after cooling. The quantity $f_{\rm aligned}$ measures the fraction of accreting gas that has $-0.1 < z/r < 0.1$ at a given $t - t_{10^5\,\rm K}$.

with the conclusion from Figs 2 and 3. In contrast, in the irregular galaxy shown in the bottom-right, there is no association between cooling and flattening. Rather, the geometry of accreting gas is quasi-spherical both before and after cooling.

Fig. 5 extends the analysis in Fig. 4 to the full sample. We parametrize the extent of flattening via a parameter $f_{\rm aligned}$ (for 'aligned accretion'), which corresponds to the fraction of accreting gas mass aligned with the disc plane ($|z/r| < 0.1$, marked by dashed vertical lines in Fig. 4). The left-hand panel of Fig. 5 shows the evolution of $f_{\rm aligned}$ from 200 Myr before $t_{10^5\,\rm K}$ (red) to 200 Myr after $t_{10^5\,\rm K}$ (blue), while the right-hand panel shows the change in $f_{\rm aligned}$ between these two epochs. The horizontal axes plot the fraction of young stars in a thin disc $f_{\rm thin\,disk,\,recent}$. For most haloes, the accreting gas is largely unaligned prior to cooling, with $f_{\rm aligned} \sim 0.1$–0.2 comparable to $f_{\rm aligned} = 0.1$ expected for an isotropic distribution. Upon cooling, the alignment of accreting gas sharply increases in haloes with $f_{\rm thin\,disk,\,recent} > 0.6$ – in most cases $\gtrsim 50$ per cent of mass collapses to $|z/r| < 0.1$ during this time. In contrast, in haloes with $f_{\rm thin\,disk,\,recent} \approx 0$, there is practically no change in $f_{\rm aligned}$ upon cooling. Intermediate cases with $f_{\rm thin\,disk,\,recent} \approx 0.2 - 0.6$ typically show a modest increase in $f_{\rm aligned}$. The right-hand panel of Fig. 5 demonstrates the strong correlation between change in $f_{\rm aligned}$ during gas cooling and the fraction of recent stars in a thin disc. That is, this panel shows that flattening is concurrent with cooling in accretion on to thin-disc galaxies, while no such association exists for accretion on to irregular or thick-disc galaxies.

The galaxy circled in the right-hand panel, `m12m`, has a stellar bar (Debattista et al. 2019), which tends to decrease $f_{\rm thin\,disk,\,recent}$. This bar may help explain why this galaxy is somewhat offset to low $f_{\rm thin\,disk,\,recent}$ relative to other galaxies with a similar large change in $f_{\rm aligned}$.

3.4 Angular momentum and energetics of accreting gas

The mechanics of concurrent cooling and flattening in rotating cooling flows is explored in Fig. 6, for the example case of `m12i`. The shaded region in panel (A) shows the 16th–84th percentiles in $j_z/|\vec{j}|$, the ratio of angular momentum in the z direction to the magnitude of total angular momentum, for individual particles as a function of $t - t_{10^5\,\rm K}$. The dashed line plots $(\Sigma\vec{j})_z/|\Sigma\vec{j}|$, i.e. the same ratio but for the total angular momentum of accreting gas at a given $t - t_{10^5\,\rm K}$. Note that this latter ratio is not identical to unity because the z direction is with respect to the central galaxy rather than the gas itself. At $t - t_{10^5\,\rm K} = -500$ Myr, the ratio $j_z/|\vec{j}|$ spans a large range of $\approx$–0.3–0.9, while by $t = t_{10^5\,\rm K}$ nearly all the accreting gas has $j_z \approx |\vec{j}|$, indicating all hot accreting gas particles are co-rotating. On the other hand, the alignment of the total angular momentum is nearly constant with time prior to accretion. These trends indicate that components unaligned with the net angular momentum are canceling out due to interaction in the hot halo.

Fig. 6 panel (B) shows the magnitude of the specific angular momentum ($|\vec{j}|$; green) and the z-component of the specific angular momentum (j_z; purple). The median value of $|\vec{j}|$ decreases prior to cooling, from $\approx$5000 kpc km s^{-1} to $\approx$ 3000 kpc km s^{-1}, in contrast with j_z which remains constant. The nearly constant j_z indicates the inflow roughly conserves its net angular momentum. At the same time the decreasing $|\vec{j}|$ indicates the inflow is cancelling out unaligned components, consistent with the conclusion from panel (A). We note that this result appears contradictory to the result of Stevens et al. (2017) based on the EAGLE simulations, which found a $\gtrsim 50$ per cent decrease in net angular momentum when accreting hot gas cools on to the galaxy.

The value of $j_z \approx 2500$ kpc km s^{-1} is comparable to the average-specific angular momentum of $j_{\rm DM} \simeq \sqrt{2}\lambda r_{\rm vir} v_{\rm vir}$ expected in dark

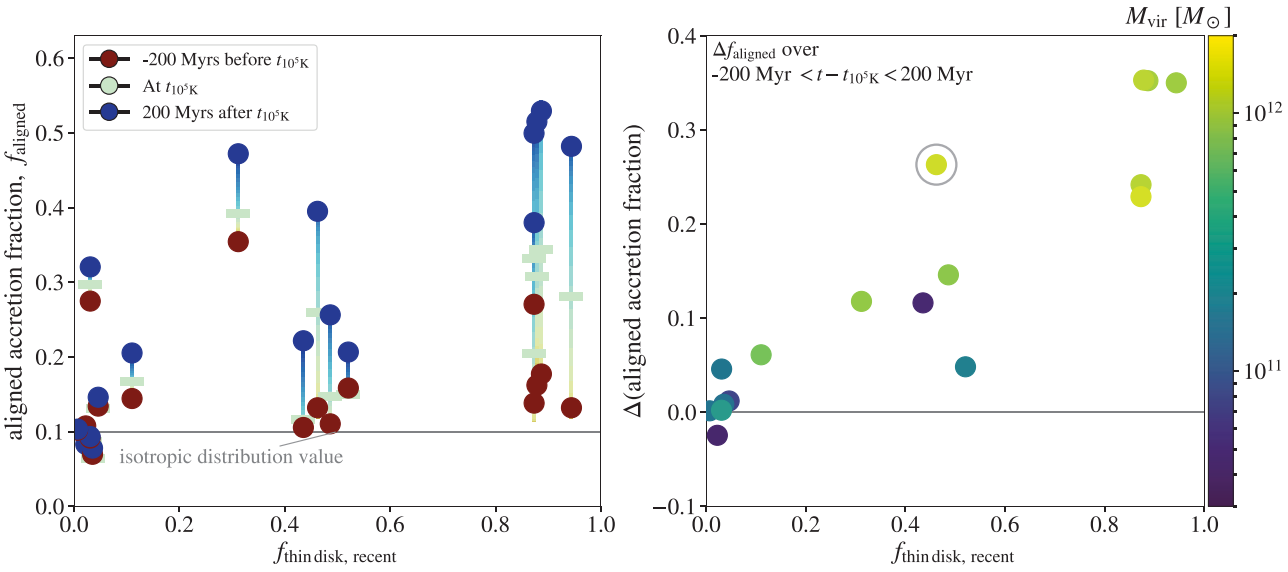

Figure 5. Left: mass fraction of accreting gas aligned with the disc ($|z/r| < 0.1$|, see Fig. 4) before and after cooling, for our sample of 17 FIRE haloes. The horizontal axis plots the fraction of young stars in the central galaxy that are in a thin disc. **Right:** change in aligned mass fraction during the ±200 Myr around cooling time shown in the left-hand panel. A large $\Delta f_{\mathrm{aligned}}$ indicates that flattening is concurrent with cooling. Colour indicates virial mass. The value of $\Delta f_{\mathrm{aligned}}$ is strongly correlated with the fraction of young stars in a thin disc. The point circled on the right is `m12m`, which has developed a sizable bar at late times.

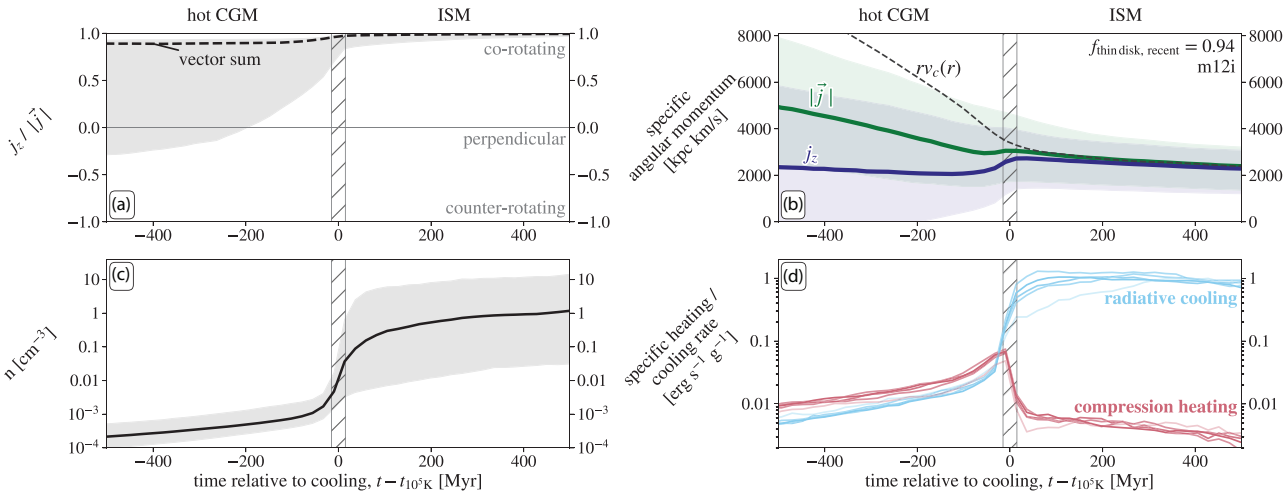

Figure 6. Angular momentum and energetics of gas accreting on to the $z \sim 0$ thin-disc galaxy (`m12i`) shown in Fig. 3, versus time relative to the final cooling time. (a) The ratio $j_z/|\vec{j}|$. The shaded regions plots the 16th–84th percentile range of the accreted particles, while the dashed line plots the vector sum. The shaded region shrinks as gas flows inward, indicating the flow becomes more coherent and that angular momentum unaligned with the total angular momentum is cancelled out. (b) The magnitude of the specific angular momentum of particles ($|\vec{j}|$, green) and the component of angular momentum aligned with the galaxy disc (j_z; purple). Solid lines and shaded regions mark the medians and 16th–84th percentile ranges, respectively. The dashed line shows the angular momentum necessary for rotational support. Cooling occurs when angular momentum support becomes significant, as expected in subsonic cooling flows (Cowie et al. 1980; Stern et al. 2020). (c) Baryon number density. Prior to cooling the gas density increases due to the inflow. As the gas cools the density sharply increases, due to the deceleration of the inflow at the galaxy scale and the collapse into a disc geometry. (d) Radiative cooling (blue) and heating from *PdV* work on accreting gas particles (red). Only gas with $T > 10^{4.5}$ K is included. In the CGM compression, heating offsets radiative cooling. This yields the mostly flat temperature profile seen in Fig. 3, as expected in a cooling flow.

matter haloes due to tidal torques (e.g. Bullock et al. 2001). Using a typical dimensionless spin parameter $\lambda \simeq 0.035$, and the virial radius $r_{\mathrm{vir}} = 270$ kpc and virial velocity $v_{\mathrm{vir}} = 130$ km s^{-1} of this halo, we get $j_{\mathrm{DM}} \approx 1750$ kpc km s^{-1}, i.e. the expected average value of the dark matter is within 30 per cent of the net angular momentum of accreting hot gas shown in Fig. 6. The fact that the gas has slightly more angular momentum than naively expected for the dark matter is consistent with previous findings that gas typically has a slightly higher spin than dark matter (e.g. Stewart et al. 2017).

The dashed line in panel (B) of Fig. 6 plots the median-specific angular momentum necessary for gas to be fully supported by angular momentum at a given radius, i.e. $rv_c(r)$. The accretion attains significant angular momentum support as it proceeds through the inner CGM, consistent with other analyses of CGM rotational support, which finds that rotation support is more prominent at

smaller CGM radii (Oppenheimer 2018; Trapp et al. 2021). The values of j_z and $v_c(r)r$ converge shortly after $t = t_{10^5\,\mathrm{K}}$, indicating that cooling and a transition to rotational support occur almost simultaneously, as indicated also by Fig. 3. This result is consistent with 1D steady-state cooling flow solutions that include angular momentum – these solutions demonstrate that the hot inflow cools to $\sim 10^4$ K at the radius where $j_z = r v_c(r)$, as long as the flow remains subsonic down to this radius (Cowie et al. 1980; Stern et al. 2020).

There is a small but noticeable increase in j_z at $t \approx t_{10^5\,\mathrm{K}}$, i.e. the angular momentum of accreting gas increases somewhat when it transitions from the hot CGM to the ISM. This increase is similar to the observed 30 per cent difference between the rotation velocity of the MW disc and its hot CGM (Hodges-Kluck, Miller & Bregman 2016). While this increase is not the focus of our analysis, we note that it may be a result of a difference in orientation between the angular momentum of the galaxy and the angular momentum of the accreting gas (e.g. Danovich et al. 2012; DeFelippis et al. 2017), which forces the accreting gas to co-rotate with the galaxy upon accretion. Any angular momentum gained is expected to be lost by other particles, driving an inflow in the disc or disc–halo interface (Mayor & Vigroux 1981; Pezzulli & Fraternali 2016).

Fig. 6 panel (C) shows the distribution of the accreting gas density versus time relative to cooling. Prior to cooling the gas density increases steadily due to the inflow, reaching $\approx 10^{-3}$ cm^{-3} just before cooling at $t \lesssim t_{10^5\,\mathrm{K}}$. This density is comparable to observational estimates of the hot gas density just outside the MW disc (e.g. Li & Bregman 2017). At $t \approx t_{10^5\,\mathrm{K}}$, the gas density sharply increases, reaching 0.1 cm^{-3} within $\approx$50 Myr, due to the decreasing radial velocity of the inflow upon accretion (Fig. 3), and due to the collapse from a quasi-spherical geometry into a disc geometry. The gas then starts forming stars shortly after cooling (Fig. 3). Note that star formation occurs despite that the 84th density percentile after cooling is $\approx$10 cm^{-3}, well below the minimum density for star formation of $n_{\mathrm{SF}} = 1000$ cm^{-3} in FIRE. This is because gas remains at densities approaching n_{SF} only for a short time before forming stars.

In Fig. 6 panel (D), we assess the energetics of the hot gas to determine why it cools. We study the energetics through two types of change in specific energy: radiative cooling (blue lines) and compression heating (red lines). Radiative cooling per unit mass for an individual particle is calculated as $n_{\mathrm{H}}^2 \Lambda / \rho$, where n_{H} is the hydrogen density, ρ is the mass density, and Λ is the cooling function. We include only fluid elements with $T > 10^{4.5}$ K to avoid optical thickness effects on cooling, and to avoid large fluctuations when Λ approaches zero at $T \approx 10^4$ K. As our focus is the energetics of the hot $\sim T_{\mathrm{vir}}$ gas, this cut does not affect our conclusions. Compression heating per unit mass for an individual resolution element is calculated as $P \frac{dV}{dt} \approx \frac{P}{\rho^2} \frac{\Delta\rho}{\Delta t}$, where P is the thermal pressure, V is the specific volume, $\Delta\rho$ is the change in density from one snapshot to the next, and Δt is the snapshot time spacing. Because accreting gas elements interact with other accreting gas elements thermodynamically, we show the mean-specific energy tracks of all gas elements binned into 100 Myr bins of $t_{10^5\,\mathrm{K}}$. Also, to focus on the behaviour of the majority of the particles, we do not bin the 1 per cent of particles with the highest change in specific energy. Some $t_{10^5\,\mathrm{K}}$ bins contain much more accreting gas than others, and to reflect this we set the darkness of the lines proportional to the number of particles in the bin.

At $t - t_{10^5\,\mathrm{K}} = -500$ Myr, the radiative cooling rate is $\approx$0.006 erg s^{-1} g^{-1}, corresponding to a cooling time $t_{\mathrm{cool}} = 400$ Myr for the median temperature of $T = 4 \times 10^5$ K at this epoch (see Fig. 3, panel A). At later $t - t_{10^5\,\mathrm{K}}$ but still prior to cooling, the radiative cooling rate increases due to the increase in gas density. The panel shows that this energy loss to radiation is followed closely by compressive heating, explaining the roughly flat temperature profile at $t < t_{10^5\,\mathrm{K}}$ (Fig. 3). This approximate equality between radiative cooling and compressive heating is a defining characteristic of classic cooling flows in which angular momentum support can be neglected (Mathews & Bregman 1978; McNamara & Nulsen 2007; Stern et al. 2019). This balance between radiative cooling and compressive heating is not possible in a perfectly hydrostatic halo, since without inward movement compression will not occur.

Around $t_{10^5\,\mathrm{K}}$, the cooling rate and compressive heating diverge. This can be understood by noting that the radiative cooling rate per unit mass scales as $\propto \rho\Lambda$, while the compressive heating rate scales as $\propto T d\log\rho/dt$. The deceleration of the hot inflow prior to accretion on to the galaxy causes ρ to increase faster than $d\log\rho/dt$, causing radiative cooling to exceed compressive heating and the temperature to decrease. This in turn increases the cooling rate, which further accelerates the drop in temperature. The result is gas that cools from $\approx 10^6$ to $\approx 10^4$ K over the course of $\lesssim$50 Myr.

Panel D also shows that after $t_{10^5\,\mathrm{K}}$ when the gas is part of the ISM, radiative cooling greatly exceeds compression heating, indicating that hot gas in the ISM is short lived.

3.5 Comparison of accretion on to thin-disc galaxies and on to irregular galaxies

Fig. 7 compares the properties of accretion on to galaxies with $f_{\mathrm{thin\,disk,\,recent}} > 0.6$ ('thin-disc galaxies') versus accretion on to galaxies with $f_{\mathrm{thin\,disk,\,recent}} < 0.6$ ('irregular galaxies'). For each property, the coloured lines show the median of the medians of the individual simulations in the group at a given $t - t_{\mathrm{acc}}$. The properties are plotted as a function of time relative to the time at which gas accretes on to the main galaxy (t_{acc}), defined as the first time gas is within r_{gal} and with a density $n_{\mathrm{H}} > 0.13$ cm^{-3}. This is in contrast with plotting properties versus $t_{10^5\,\mathrm{K}}$ as done above, since in irregular galaxies where accretion is generally cool ($T \approx 10^4$K), the last cooling time is not associated with accretion on to the galaxy. We also exclude `m12f` from the thin-disc group since the gas cools and becomes rotationally supported at significantly larger radii than r_{gal}, due to the exceptionally large $j_z \approx 5000$ kpc km s^{-1} of hot gas in this galaxy. This galaxy is further discussed in Appendix D (online).

The red lines in Fig. 7 demonstrate that the conclusions from Figs 3 and 6 hold on average for all thin-disc galaxies in our sample: gas inflow is hot through the CGM with a median $T \approx 10^{5.5}$ K, and cooling and deceleration occurs at the galaxy edge, at which time the gas distribution also flattens. In contrast, accretion on to irregular galaxies is primarily cold, with no change in median temperature before and after accretion. Gas becomes more spatially aligned as it accretes, but still has a median $|z|/r \sim 0.2$, and never becomes fully rotationally supported. Accretion on to thin discs and irregulars also differ significantly in their spin-aligned fraction prior to t_{acc} (lower-left panel) – at t_{acc} the fraction of spin-aligned accretion on to thin-disc galaxies is 0.75, a factor of 3 higher than the fraction of 0.25 in irregular galaxies. This suggests that achieving angular momentum coherence in the CGM is conducive to the formation of thin discs.

3.6 Angular momentum coherence in accreted gas

Fig. 8 shows the evolution of the angular momentum distribution for `m12i` versus time relative to t_{acc}. We use an 'on-sky' azimuthal equidistant projection of the angular momentum direction for `m12i`. Azimuthal equidistant projections preserve the distance to the central

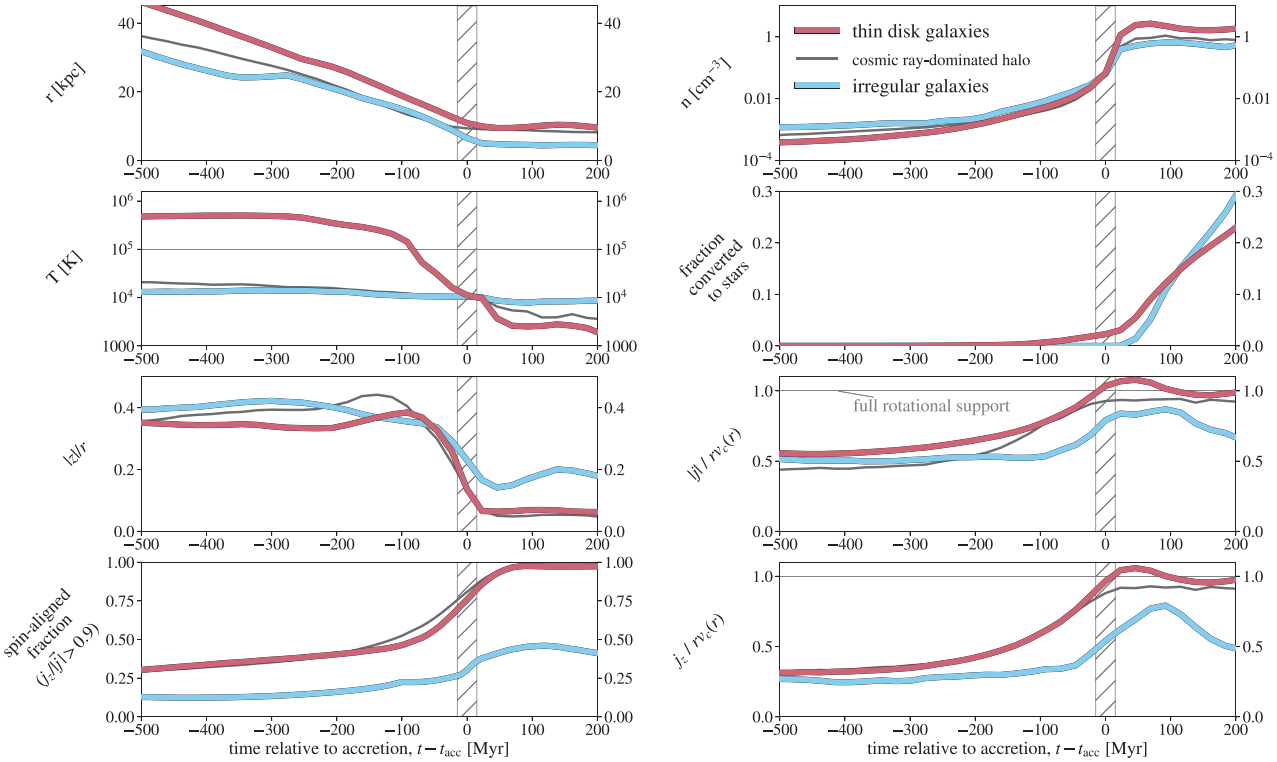

Figure 7. Hot accretion on to thin-disc galaxies versus cool accretion on to irregular galaxies. Lines plot the median properties of the accreting gas relative to time of accretion, for thin-disc galaxies (red; $f_{\rm thin\,disk,\,recent} > 0.6$) and for irregular galaxies (blue; $f_{\rm thin\,disk,\,recent} < 0.6$). The temperature panel (second row on the left) shows that accretion on to thin-disc galaxies is hot ($T \gtrsim 10^{5.5}$ K), in contrast with cool $T \approx 10^4$ K accretion on to irregular galaxies. The bottom panels show that accretion on to thin-disc galaxies also has an angular momentum distribution that is more aligned and is more rotationally supported than in irregular galaxies, suggesting that the coherence achieved in hot accretion is conducive to the formation of galaxy discs. The dark grey lines show the median accretion properties in a CR-dominated halo. The accretion in this halo is cool, but similar in its angular momentum properties to hot accretion (see Section 4.4).

point (the angular momentum direction of the galaxy at $z = 0$) as well as the orientation (ϕ) relative to the central point. Each histogram bin covers an equal area. The total angular momentum of the accreting gas at each time $\Sigma\,\vec{j}$ is shown via a black point outlined in white. The figure shows that prior to $t - t_{\rm acc} = -500$ Myrs, accretion is composed of gas rotating in a variety of directions, including counter-rotating ($j_z/|j| < 0$ or equivalently $\theta > 90°$). The net angular momentum $\Sigma\,\vec{j}$ is, however, roughly centred on the angular momentum of the galaxy $\theta = 0°$. By $t - t_{\rm acc} = -50$ Myrs, the angular momentum distribution is significantly more coherent/narrower, while only a minor change in seen in the direction of net angular momentum vector. At and shortly after $t_{10^5\,\rm K}$, the angular momentum distribution further narrows and the net vector nearly fully aligns itself with the galaxy.

Fig. 9 shows the cumulative distribution function of $j_z/|\vec{j}|$ in the accreted gas, weighted by mass, for the four simulations shown in Fig. 4. This distribution quantifies the level of alignment of angular momentum in the accreted gas with respect to the rotation axis of the stars. For reference, perfectly co-rotating gas has $j_z/|\vec{j}| = 1$, while perpendicular and counter-rotating gas have $j_z/|\vec{j}| = 0$ and -1, respectively. An isotropic distribution of angular momentum would appear as a diagonal line in this plot. Each curve corresponds to a different $t - t_{\rm acc}$ as noted in the legend. Outlined in black are the CDFs for $t - t_{\rm acc} = -200$, 0, and 200 Myr.

In gas accreting on to thin-disc galaxies (top and bottom-left panels of Fig. 9), the angular momentum distribution becomes increasingly coherent with time relative to $t_{\rm acc}$. At $t - t_{\rm acc} = -1$ Gyr, the angular momentum distribution is marginally coherent, with $\approx 50 - 70$ per cent of accreting gas co-rotating with $j_z/|\vec{j}| > 0.5$. In contrast at $t - t_{\rm acc} = +200$ Myr, the distribution is highly coherent, with $j_z/|\vec{j}| > 0.9$ for $\gtrsim 90$ per cent of accretion. The majority of the evolution in coherence occurs over $\lesssim$200 Myr prior to $t_{\rm acc}$, as seen by the differences between the distributions for $t - t_{\rm acc} = -200$ Myr and $t - t_{\rm acc} = 0$ Myr. This increase in coherence allows the accreting gas to collapse into a thin disc as shown in Figs 4 and 5. Furthermore, this result shows that accreting gas is almost entirely co-rotating with the galaxy *prior* to accreting, i.e. while the accretion is still part of the galactic 'hot corona'.

In stark contrast with thin-disc galaxies, the irregular galaxy `m11d` shown in the bottom-right panel of Fig. 9 experiences only a very mild evolution in angular momentum coherence – angular momentum remains only marginally co-rotating both before and after accreting.

In Fig. 10, we show the change in angular momentum alignment across the full sample, similar to Fig. 5 for spatial alignment. In this case, spin alignment is defined as the fraction of gas with $j_z/j > 0.9$. The change in spin alignment is calculated focusing on the time prior to accretion, -1 Gyr $< t - t_{\rm acc} < 0$ Gyr. The figure shows a correlation between thin-disc fraction and the increase in angular momentum alignment prior to accretion, suggesting that achieving angular momentum coherence in the CGM is conducive to the formation of thin discs.

4 DISCUSSION

In this paper, we analyse the properties of gas accreting on to $z \sim 0$ galaxies simulated in FIRE, focusing on Milky-Way mass galaxies in which new stars form in a thin disc. We find that thin-disc galaxies

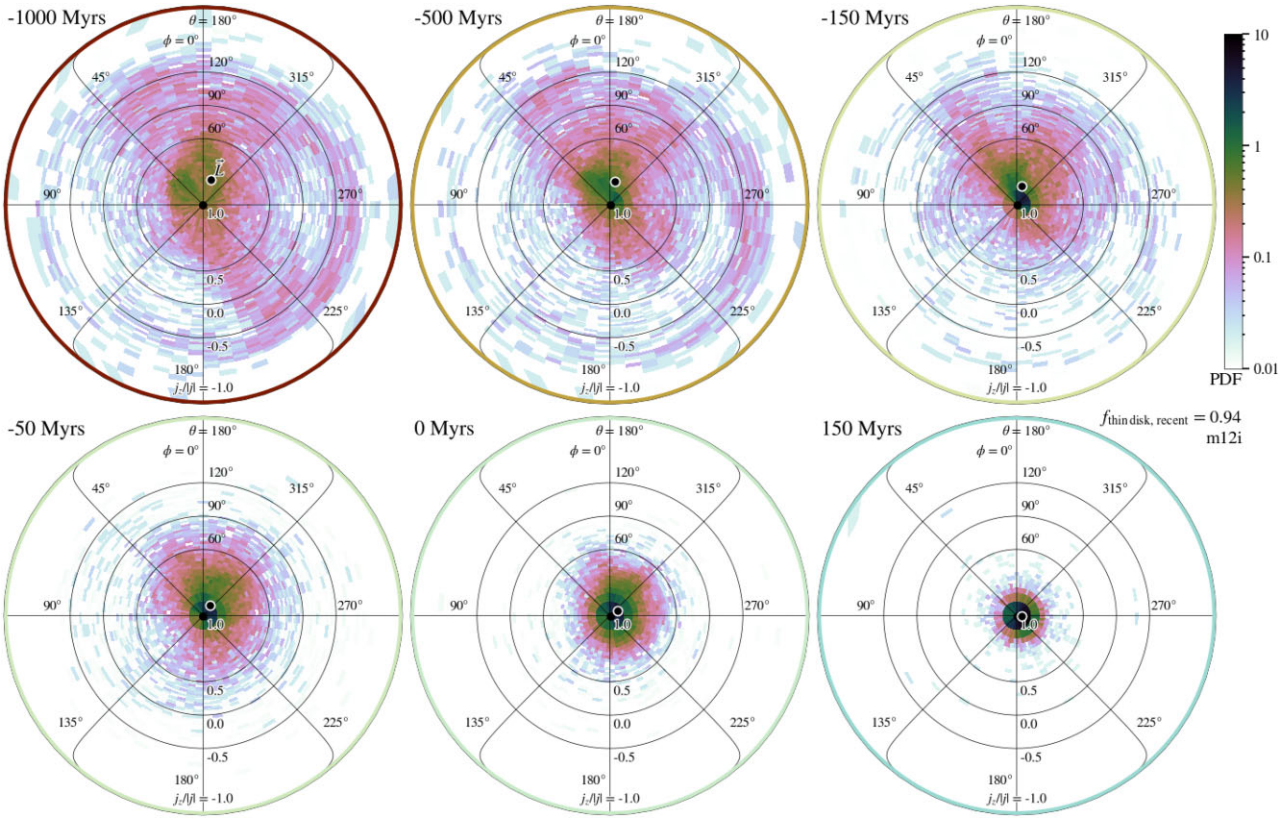

Figure 8. The evolution of the direction of angular momentum for gas accreting on to a MW-like galaxy, `m12i`, in an 'on-sky' projection. Different panels show the distribution for different times relative to $t_{\rm acc}$. The bin colour is logarithmically proportional to the fraction of accreting mass with an angular momentum pointing in that direction. The angles θ and ϕ are spherical coordinates where $\theta = 0^\circ$ is the direction of the galaxy angular momentum at $z = 0$ (shown in the centre of the projection). The black point outlined in white is the direction of the net angular momentum vector of accreting gas, $\Sigma\,\vec{j}$. Over the course of 1 Gyr prior to accreting the angular momentum distribution narrows significantly (i.e. becomes more coherent), while the direction of the net vector changes only slightly.

in FIRE accrete via 'rotating cooling flows', which is a type of 'hot accretion'. In this accretion mode, the quasi-spherical $T \sim T_{\rm vir}$ CGM phase inflows towards the galaxy, remaining hot down to the radius where its angular momentum is sufficient to provide rotational support. At this radius ($\gtrsim 4 r_{\star,\,0.5}$, just outside the galaxy radius), the hot inflow both decelerates and becomes coherently rotating, and then simultaneously cools and collapses into a rotating cool disc. Our results thus extend classic cooling flow theory by demonstrating their applicability in realistic cosmological simulations, and by exploring the mechanics of cooling flows with angular momentum, a subject which has not yet been studied extensively (cf. Cowie et al. 1980; Stern et al. 2020). Moreover, we find a strong correlation between the prevalence of this accretion mode and the fraction of stars in the central galaxies that form in a thin disc, potentially indicating that a rotating cooling flow is a necessary condition for the formation of a thin star-forming disc. In this section, we discuss several interpretations, caveats, and implications of our results.

4.1 Why are rotating cooling flows conducive to thin-disc formation?

A main result of our analysis is that when accretion occurs via rotating cooling flows, the accreted gas forms a coherently rotating disc *prior* to cooling and accreting on to the ISM. This is due to the decrease in angular momentum dispersion prior to cooling (Figs 8–10, and panels A and B in Fig. 6) and due to the deceleration of the flow prior to accretion (panel D in Fig. 3). Combined, these two properties indicate that upon accretion the flow is already in a coherent disc with $v_\phi \approx v_{\rm c}$ and v_r, $v_z \ll v_{\rm c}$. In contrast, in other accretion modes (such as cold streams and precipitation), the inflow may reach the ISM with a large dispersion in angular momentum and substantial radial momentum, so equilibration will start only after accretion on to the ISM. That stars in FIRE galaxies, which are fed by cool accretion form in irregular distributions for many Gyrs (Figs 7 and D1), suggest that equilibration in the ISM alone may be insufficient to form a thin disc, and hence equilibration in the CGM, as we find in galaxies fed by rotating cooling flows is conducive to the formation of thin discs.

Why is equilibration in the ISM alone insufficient to form a thin disc in FIRE? Equilibration is expected to proceed on a dynamical time-scale (∼100 Myr), which is short relative to the star formation time-scale of ∼0.5–2 Gyr (e.g. fig. 3 of Bigiel et al. 2008). However, some stars may succeed in forming while the accreting gas morphology is still a thick disc or irregular. Such stars inject feedback momentum and energy into their surroundings, which could further delay the equilibration process, allowing even more stars to form outside of a thin disc.

The tendency of hot inflows to decelerate and rotate coherently prior to accretion is potentially a result of the subsonic nature of the flow. In a subsonic flow, gradual deceleration prior to accretion is expected since the inflow is 'forewarned' (via changes in pressure) of the transition to rotational support at the galaxy scale. This is in contrast with supersonic accretion modes where the accreting gas

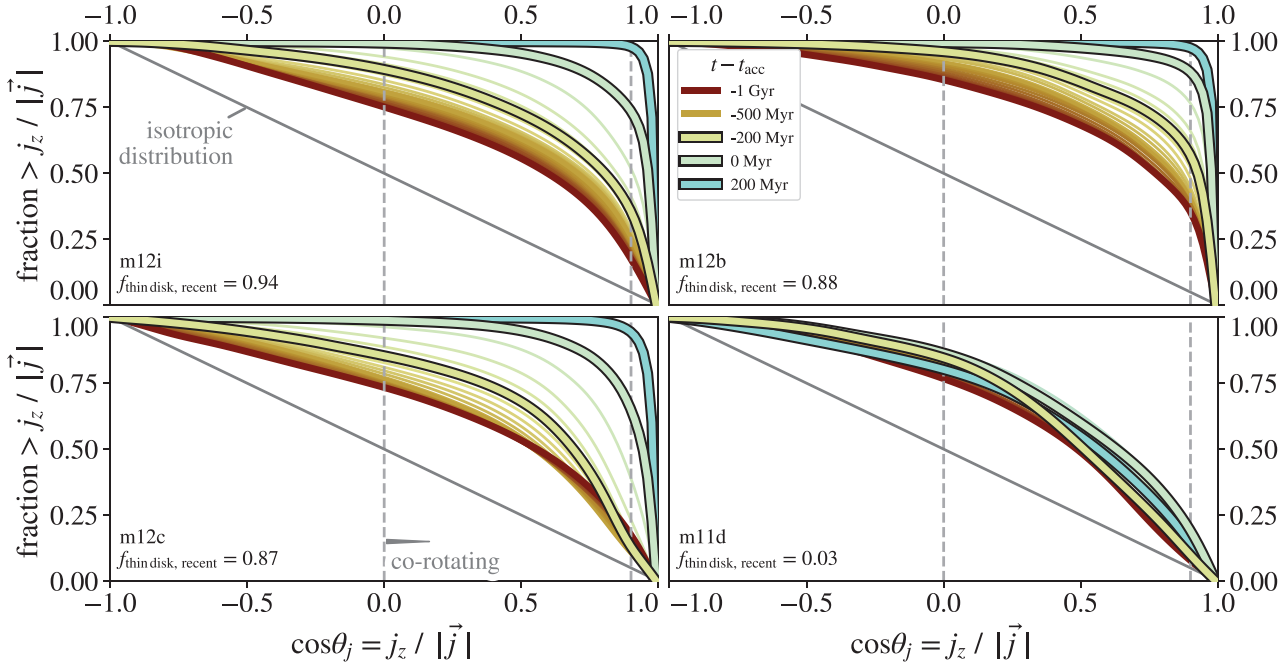

Figure 9. Angular momentum distribution of accreting gas, as a function of time relative to accretion time. The galaxies displayed are the same as in Figs 1 and 4. Curves show the fraction of mass above a given $j_z/|\vec{j}|$. In the thin-disc galaxies (top and bottom-left panels), the angular momentum distribution becomes more coherent and aligned with the central galaxy with time, especially during the 200 Myr prior to accretion. In the irregular galaxy (bottom right), the angular momentum distribution is only mildly co-rotating both before and after accreting.

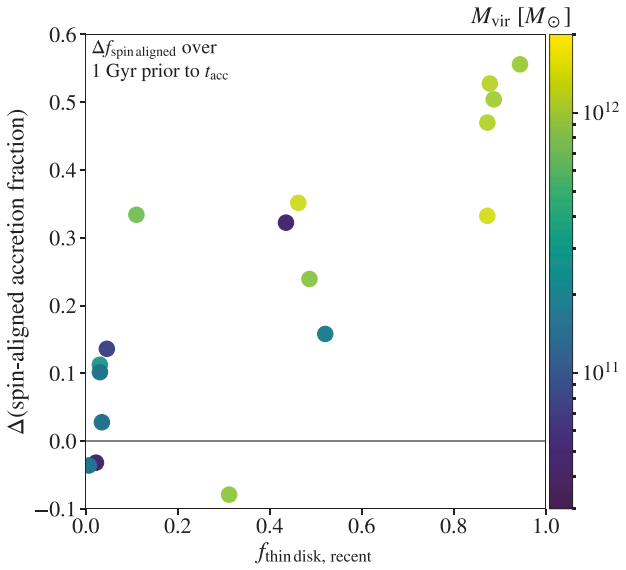

Figure 10. The change in the fraction of accreting gas mass, which is spin-aligned with the galaxy ($j_z/|\vec{j}| > 0.9$, right dashed lines in Fig. 9) over 1 Gyr prior to accretion, versus thin-disc fraction for the full sample of simulations. This figure is an angular momentum-space equivalent to the change in geometry shown in the right-hand panel of Fig. 5. The strong correlation between change in spin-alignment and thin-disc fraction suggests that achieving angular momentum coherence in the CGM is conducive to the formation of thin discs.

is expected to shock and halt abruptly at the galaxy scale. Also, subsonic accretion makes it easier for the flow to reach angular momentum coherence, since the inflow time-scale is longer than the sound-crossing time-scale on which coherence can be achieved. In contrast, in supersonic, free-falling accretion flows as we find in low-mass galaxies, the accretion and coherence time-scales are both comparable to the dynamical time and hence comparable to each other, so coherence is not achieved in the CGM.

Panels A–B in Fig. 6 and Figs 8–10 demonstrate that angular momentum coherence is achieved in hot inflows just before cooling and accretion, roughly at the rotational support radius r_{circ} (defined via $\Sigma\vec{j} = v_c(r_{circ})r_{circ}$, where $\Sigma\vec{j}$ is the net angular momentum in the flow), rather than farther out in the halo. Since the hot inflow is subsonic at all radii, this result suggests that a dynamical time-scale longer than the sound-crossing time-scale is not, on its own, a sufficient condition for the flow to achieve angular momentum coherence. We suspect that coherence is achieved specifically near r_{circ} because of the relation between average rotation speed and subsonic turbulence in the hot CGM, where the latter is driven by e.g. clumpy cosmological accretion, stirring by subhalos, and feedback from the galaxy. To understand this, we can look at the relative magnitude of angular momentum fluctuations due to turbulence $\sigma_{turb}r/j_z$, where σ_{turb} is the turbulent velocity. For subsonic turbulence with a mach number of say $\mathcal{M}_{turb} = 1/3$, we have $\sigma_{turb} \approx \mathcal{M}_{turb}v_c$, since the sound speed in hot inflows is roughly equal to v_c. Combining this with the definition of r_{circ} and the conservation of j_z in the inflow (Fig. 6, panel B), we get that angular momentum fluctuations are of order $r\sigma_{turb}/j_z \approx \mathcal{M}_{turb}r/r_{circ}$. Thus, for subsonic turbulence, the relative magnitude of angular momentum fluctuations will be small at $r \approx r_{circ}$, but could be large at larger radii, as found above. We defer further exploration of this potential relation between turbulence and angular momentum coherence to future work.

We note that accretion via a rotating cooling flow does not ensure a thin disc forms. A merger, a strong feedback event, or other disruptions may take a thin gaseous disc and disturb it, preventing stars from forming in a thin disc. Simulation `m12m` provides an example of this: it has rotating cooling flow accretion comparable

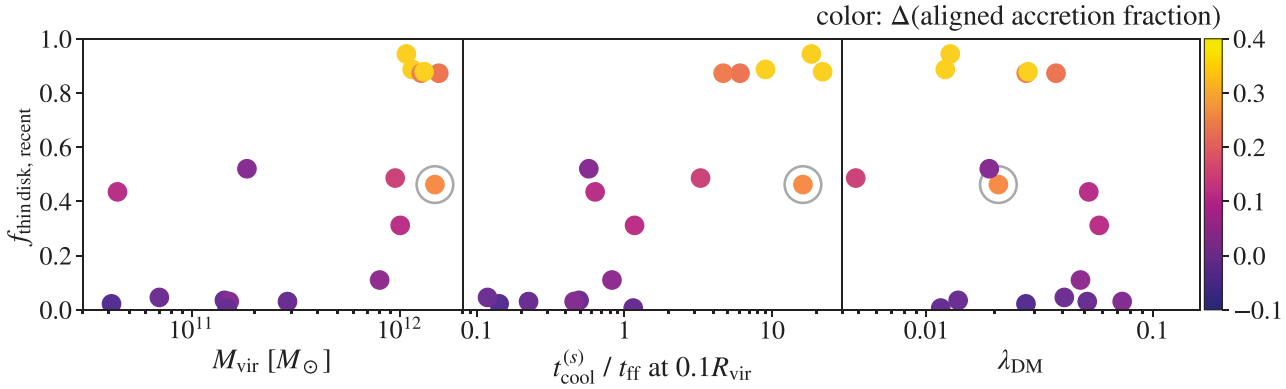

Figure 11. Fraction of young stars in a thin disc versus $M_{\rm vir}$ (left), versus $t_{\rm cool}^{(s)}/t_{\rm ff}$ evaluated at $0.1R_{\rm vir}$ (middle), and versus dark-matter spin parameter (right). Markers are coloured by $\Delta f_{\rm aligned}$, a measure of the dominance of rotating cooling flows in accreting gas (Fig. 5). The middle panel shows that thin discs appear in haloes with $t_{\rm cool}^{(s)} \gg t_{\rm ff}$, while irregular galaxies appear in haloes with $t_{\rm cool}^{(s)} \lesssim t_{\rm ff}$. This relation further supports our conclusion that rotating cooling flows are conducive to the formation of thin discs, since a rotating cooling flow is expected after the inner CGM virializes, which occurs when $t_{\rm cool}^{(s)}$ exceeds $t_{\rm ff}$ at $0.1R_{\rm vir}$ (Stern et al. 2021b).

to thin-disc galaxies ($\Delta f_{\rm aligned} \approx 0.25$), but has a relatively small $f_{\rm thin\,disk,\,recent} \approx 0.5$ (circled point in Fig. 5) due to the presence of a bar. However, the strong correlation seen in Fig. 5 between the prevalence of rotating cooling flow accretion (quantified via $\Delta f_{\rm aligned}$) and the thin-disc fraction $f_{\rm thin\,disk,\,recent}$ suggests that such events are relatively rare.

4.2 When and where do we expect thin discs?

The scenario suggested by this paper that thin star-forming discs are a result of accretion via rotating cooling flows allows us to predict at which halo masses and redshifts we expect thin discs to form. At low redshift, cooling flows are expected if a time-steady and pressure-supported 'virialized CGM' has formed, which occurs when the cooling time of hot shocked CGM gas $t_{\rm cool}^{(s)}$ exceeds the free-fall time $t_{\rm ff}$, typically at halo masses above a threshold of $\sim 10^{11}$–10^{12}M$_\odot$ (e.g. White & Rees 1978; White & Frenk 1991; Birnboim & Dekel 2003). The existence of cooling flows also requires that radiative cooling in this hot gas is not balanced by feedback. While there is evidence for feedback balancing radiative cooling in group and cluster haloes, at which the cooling rate implied by X-ray observations greatly exceeds the central galaxy SFR (i.e. haloes with a 'cooling flow problem'; see McDonald et al. 2018 for a recent study), there is no similar evidence for a cooling flow problem in the haloes of disc galaxies (Li, Crain & Wang 2014), though uncertainties are still large due to the weak X-ray emission from the hot gas at this mass scale. Cooling flows in the low redshift universe are thus possible at intermediate masses, where on one hand the halo is massive enough so the CGM has virialized, but on the other hand, the halo is not so massive that X-ray observations rule them out.

Stern et al. (2020) recently refined the classic condition for the existence of cooling flows by showing that even if a virialized CGM exists in the outer halo the resulting cooling flow may go through a sonic point and reach the galaxy as cool supersonic accretion. Thus, to produce cooling flows that remain hot and subsonic down to the galaxy scale as found above for thin-disc galaxies, a more specific condition should be satisfied, namely that $t_{\rm cool}^{(s)}$ exceeds $t_{\rm ff}$ at an inner CGM radius of $\approx 0.1 r_{\rm vir}$, i.e. subsonic cooling flow requires that the *inner* CGM is virialized. In our simulation sample, the condition $t_{\rm cool}^{(s)} \gtrsim t_{\rm ff}$ at $\approx 0.1 r_{\rm vir}$ is met at $M_{\rm vir} \approx 10^{12}$ M$_\odot$ (Stern et al. 2021b). Fig. 11 shows the relationship between thin-disc fraction and virial mass (left-hand panel), $t_{\rm cool}^{(s)}/t_{\rm ff}$ at $0.1 r_{\rm vir}$ (middle panel), and dark-matter spin parameter in our sample of $z \sim 0$ FIRE galaxies. Markers are coloured by $\Delta f_{\rm aligned}$, a measure of the dominance of rotating cooling flows in accreting gas (Fig. 5). The figure shows that thin discs and rotating cooling flows appear at $M_{\rm vir} \approx 10^{12}$ M$_\odot$ and $t_{\rm cool}^{(s)}/t_{\rm ff}(0.1 r_{\rm vir}) > 1$, consistent with the expectation noted above that cooling flows and hence thin discs commence only when the inner CGM virializes. This mass scale for thin-disc formation is, however, somewhat larger than in $z \sim 0$ observations, as further discussed in Section 4.5. While thin-disc fraction does correlate with mass scale, the dark-matter mass and angular momentum properties alone are likely insufficient to predict galaxy morphology, as indicated by the lack of correlation between the dark-matter spin parameter and $f_{\rm thin\,disk,\,recent}$.

How does thin-disc formation depend on redshift? While the threshold of inner CGM virialization in FIRE is roughly independent of redshift (Stern et al. 2021b, a), at $z > 1$ cold streams may penetrate the hot halo and dominate the accretion (e.g. Kereš et al. 2005; Dekel & Birnboim 2006; Dekel et al. 2009), and thus if thin discs form as a result of hot accretion, as suggested in this work, they would be rarer at high redshift. Alternatively, thin discs could be rarer at high redshift due to evolving gas fractions, since in equilibrium disc models the thickness of the disc scales with gas fraction (Thompson, Quataert & Murray 2005; Faucher-Giguère, Quataert & Hopkins 2013; Krumholz et al. 2018). These predictions are consistent with morphological and kinematic observations of galaxy samples, where thin discs are found mainly at $z < 1$ and intermediate galaxy masses (e.g. Kassin et al. 2012a; van der Wel et al. 2014).

4.3 Comparison to other models for the hot CGM

Our result that the inner CGM of Milky-Way mass galaxies forms a rotating cooling flow can be compared to other models for the hot CGM of MW-like galaxies. In both the precipitation-regulated model of Sharma et al. (2012) and Voit et al. (2017) and the isentropic model of Faerman, Sternberg & McKee (2020), the expected inflow induced by radiation is suppressed due to a balance between radiative cooling and heating by feedback ('thermal balance'), and the hot gas is in hydrostatic equilibrium. Our results based on the FIRE simulations suggest a different scenario, where the hot CGM is not in thermal balance but rather inflows on a cooling time-scale

as expected from classic cooling flow solutions. This implies that stellar feedback in Milky-Way mass galaxies in FIRE is insufficient to disrupt the cooling flow, consistent with the weak outflows at this mass and redshift scale in the FIRE simulations (Muratov et al. 2015, 2017; Anglés-Alcázar et al. 2017; Pandya et al. 2021) and in observations (e.g. Heckman & Thompson 2019). The potential effects of active galatic nucleus (AGN) feedback, not implemented in the FIRE sample used in this work, are further discussed in Section 4.5. We note though that even in cooling flows the pressure profile of the hot CGM is consistent with hydrostatic equilibrium to zeroth-order, with relatively small deviations of order $\approx(t_{\rm ff}/t_{\rm cool})^2$ (Stern et al. 2019).

Our results also differ from precipitation models in that the hot inflow *dominates* the accretion on to disc galaxies, rather than accretion by cool clouds condensed from the hot medium (Figs 7 and C1; see also Esmerian et al. 2021). We expect this dominance of hot inflows to be robust to resolution effects despite that the formation of cool clouds in simulations depends on resolution (e.g. McCourt et al. 2018; Mandelker et al. 2019, 2021; Fielding et al. 2020). This follows since the hot gas accretes on the cooling time-scale (Section 3.4), i.e. the same time-scale on which thermal instabilities grow. Thermal instabilities in an inflowing hot CGM thus do not have time to grow substantially, as indicated by idealized calculations of cooling flows (Balbus & Soker 1989; Stern et al. 2019). A systematic resolution test of this result is, however, beyond the scope of this paper.

It is also interesting to compare our results to the calculations of Pezzulli, Fraternali & Binney (2017) and Sormani et al. (2018), who considered the effect of angular momentum support on the structure of a hot CGM, which is hydrostatic except for the rotation component. Since cooling flows are also hydrostatic to zeroth-order as mentioned above, they are expected to satisfy similar constraints on their pressure profiles as in these previous models (see equation 1 in Sormani et al. 2018). Our results, however, suggest another constraint on the hot CGM structure that was not considered by these previous studies – the radial distribution of the net angular momentum is flat, since the hot CGM conserves angular momentum as it inflows (Fig. 6, panel B). We defer building idealized hot CGM models that satisfy this additional constraint to future work.

4.4 Analogous accretion in cosmic ray-dominated haloes

The dark grey line in Fig. 7 shows the median properties of accreting gas in a simulation that includes cosmic ray (CR) physics (`m12i_cr`; Chan et al. 2019; Hopkins et al. 2020), thus providing a window into the differences in gas accretion modes in simulations with CR support in the CGM. The accretion on to the central galaxy in the CR-dominated halo is similar to rotating cooling flows in many aspects: accreting gas gains coherence in the halo becomes rotationally supported at the galaxy edge (with a decreased radial velocity), and subsequently collapses into a disc. These properties were highlighted also by Trapp et al. (2021), who performed an analysis on the accretion of gas on to MW-mass disc galaxies with CR-dominated haloes. Consistent with our results, Trapp et al. (2021) found that accretion on to MW-mass discs has the same qualitative behaviour, regardless of whether or not the halo is CR-dominated. However, the top-left panel of Fig. 7 demonstrates that accreting gas in CR-dominated haloes never shocks to a temperature $T\sim T_{\rm vir}\sim 10^{5.5}$ K – instead the median temperature for the CR-dominated halo is $T\approx 10^4$ K. This is because in `m12i_cr` the CGM is not supported against gravity by thermal pressure, but rather by CR pressure (Ji et al. 2020).

Increased coherence and decreased radial velocity prior to accretion are the two properties of rotating cooling flows we identify as promoting thin-disc formation (Section 4.1), and are clearly present in `m12i_cr` (Fig. 7). Consistent with this, `m12i_cr` has a high thin-disc fraction, $f_{\rm thin\,disk,\,recent}=0.9$. In Section 4.1, we argue that the coherent co-rotation and deceleration of rotating cooling flows is a result of its subsonic nature. The accreting gas in the CR-dominated halo is also effectively subsonic – gas velocities are below the effective sound speed $c_{s,\rm eff}$ and therefore have properties characteristic of subsonic gas. The effective sound speed $c_{s,\rm eff}$ is defined as part of the local strong-coupling approximation used for the subgrid CR physics prescription, wherein the total pressure used to determine gas trajectories is a combination of hydrodynamic and CR pressure ($P=P_{\rm gas}+P_{\rm cr}$) and the sound speed is $c^2_{s,\rm eff}=c_s^2+\gamma_{\rm cr}P_{\rm cr}/\rho$ (Hopkins et al. 2020). Cool $\sim 10^4$ K accreting gas can therefore act subsonic, and thus be conducive to thin-disc formation, as long as $P_{\rm cr}$ is sufficiently large. The qualitatively similar behaviour between both rotating cooling flows and accretion in CR-dominated haloes may suggest that these accretion modes are a subset of a more general form of *disc-conducive subsonic accretion*.

4.5 Caveats

In our MW-mass haloes, the average SFR over $z=0$–0.5 is SFR $\approx 3-10\,{\rm M_\odot yr^{-1}}$, while the observationally based average SFR for $M_{\rm vir}\sim 10^{12}$ M$_\odot$ haloes over the same redshift range is a lower SFR $\approx 0.7-6\,{\rm M_\odot\,yr^{-1}}$ (Behroozi, Wechsler & Conroy 2013). Since one component that regulates the SFR is the gas accretion rate on to the galaxy, this may suggest that our simulations have higher accretion rates from the CGM on to the galaxy $\dot{M}_{\rm CGM}$ than in real galaxies at the same mass-scale. The CGM accretion rate in FIRE may be reduced if the cooling flow is disrupted by additional physics implemented in some other suites of FIRE simulations, including CRs (Chan et al. 2019; Hopkins et al. 2020, 2021c,a) and AGN feedback (Wellons et al. 2022). It is, however, unclear whether additional processes such as these can disrupt cooling flows around MW-way mass galaxies. For example, CR transport models remain highly uncertain, especially in the CGM (Hopkins et al. 2021b; Quataert, Thompson & Jiang 2021a, b), and it is not yet known how AGN feedback couples to halo gas. Moreover, if AGN feedback is intermittent, it is possible that a rotating cooling flow could reform between bursts of AGN feedback, especially at small CGM radii as analysed above where cooling and dynamical times are relatively short.

An alternative solution to the elevated accretion rate problem is that the cooling flow is not disrupted, but just weaker than in FIRE, as expected if the CGM mass or metallicity are overpredicted in FIRE at $z\sim 0$. This follows since in a cooling flow $\dot{M}_{\rm CGM}\propto M^2_{\rm CGM}\Lambda(Z_{\rm CGM})$, where $M_{\rm CGM}$ and $Z_{\rm CGM}$ are the CGM mass and metallicity, respectively, while Λ is the cooling function. Thus, if the CGM mass is overpredicted by a factor of 2 then $\dot{M}$ and the SFR would be overestimated by a factor of 4. Both the CGM mass and metallicity are a result of the integrated enrichment and depletion of the CGM by outflows over cosmic time, and thus are uncertain (e.g. Davies, Crain & Pontzen 2021; Kelly et al. 2021).

A lower CGM mass or metallicity may also help address the difference between the mass threshold for rotational support in FIRE and in observations. At $z\sim 0$, FIRE galaxies have significant rotational support ($V_{\rm rot}/\sigma_z\gg 1$) above $M_\star\sim 10^{10}$ M$_\odot$, higher than in observations which find rotationally supported galaxies above $M_\star\sim 10^9$ M$_\odot$ (Wheeler et al. 2016; El-Badry et al. 2018a,b, see also Peebles 2020). A lower $M_{\rm CGM}$ or $Z_{\rm CGM}$ would imply a higher $t^{(s)}_{\rm cool}$ and $t^{(s)}_{\rm cool}/t_{\rm ff}$ for a given halo mass, thus decreasing the mass threshold for

inner CGM virialization. The latter effect would cause the onset of cooling flows and the formation of thin discs to occur at lower halo masses than suggested by Fig. 11. At $z \sim 0$, a factor of a few increase in $t_{\rm cool}^{(s)}$ relative to that in FIRE would decrease the threshold halo mass in which the inner CGM virializes to $M_{\rm vir} \sim 10^{11}$ M$_\odot$ (Stern et al. 2021b), corresponding to a threshold stellar mass for a thin-disc formation of $M_\star \sim 10^9$ M$_\odot$ similar to the observed value.

This difference between observed and simulated CGM mass or metallicity, as well as the general picture of rotating cooling flows, can be tested by comparison with CGM observations. The analysis of Stern et al. (2019) suggests that a cooling flow model with $\dot{M}_{\rm CGM} \approx 1M_\odot$ yr^{-1}, roughly equal to the accretion rate needed to sustain star formation in the Galaxy, is consistent with X-ray absorption and emission observations in the Milky-Way CGM. Also, in line with the above scenario where FIRE somewhat overpredicts $M_{\rm CGM}$, some estimates of the CGM mass based on X-ray observations find $M_{\rm CGM}/f_b M_{\rm vir} \approx 0.1$ (Bregman et al. 2018; Li et al. 2018), where $f_b M_{\rm halo}$ is the cosmological baryon fraction multiplied by the halo mass. This is lower than $M_{\rm CGM}/f_b M_{\rm vir} \approx 0.2$–$0.4$ for similar-mass FIRE haloes (Hafen et al. 2019). However, other studies deduce a higher $M_{\rm CGM}/f_b M_{\rm halo} = 0.3$ based on the same X-ray data (Faerman et al. 2020), while Chan et al. (2021) find X-ray emission in FIRE is at the low end of the observed distribution when matching simulated and observed galaxies by their SFR. We defer a more direct comparison of the predictions of the rotating cooling flow model realized in FIRE with observations to future work.

5 SUMMARY

In this paper, we use the particle-tracking method developed in Hafen et al. (2019, 2020) to study how gas accretes on to $z \sim 0$ galaxies in the FIRE-2 cosmological zoom simulations (Hopkins et al. 2018), focusing on Milky-Way mass galaxies in which stars form in a thin disc. Our main results are as follows.

(i) **Mechanics of rotating cooling flows at $z \sim 0$:** We find that gas accretion on to thin-disc galaxies in FIRE is dominated by rotating cooling flows, wherein the hot $T \approx T_{\rm vir}$ CGM forms a subsonic and angular momentum-conserving inflow down to the galaxy–halo interface, at which it cools to $T \lesssim 10^4$ K (Figs 3 and 6). Cooling occurs at the radius where rotational support in the flow becomes substantial, and is concurrent with flattening of the flow, i.e. the flow transitions rapidly from a quasi-spherical hot medium into a cool thin disc (Figs 2 and 4). Prior to cooling and flattening, the hot flow decelerates and becomes coherently rotating with a narrow angular momentum distribution (Figs 8–10), properties which we attribute to the subsonic nature of the flow (Section 4.1). Our results thus extend classic cooling flow theory by demonstrating rotating cooling flows are a primary accretion mode for many cosmologically simulated galaxies, and by further exploring the mechanics of cooling flows with angular momentum beyond previous studies (Cowie et al. 1980; Stern et al. 2020). Also, the inflowing nature of the hot CGM phase surrounding disc galaxies in FIRE is in contrast with the common assumption that the hot CGM is static (e.g. Maller & Bullock 2004; Sharma et al. 2012; Faerman, Sternberg & McKee 2017; Voit et al. 2017; Faerman et al. 2020).

(ii) **Relation between rotating cooling flows and thin stellar discs:** We find that across a sample of 17 galaxies spanning 10^8 M$_\odot$ $< M_\star < 10^{11}$ M$_\odot$, there is a strong correlation between the dominance of cooling flow accretion and the fraction of stars formed in a thin disc in the central galaxy (Figs 4–5, 10). This expands the result of Stern et al. (2021b), which found a relation between the formation of discs and the virialization of the inner CGM in FIRE, where the latter is a necessary condition for the onset of cooling flows. We theorize that rotating cooling flows are conducive to the formation of thin discs since these flows achieve coherent, purely rotating kinematics prior to cooling to $\lesssim 10^4$ K, and thus before any star formation in the accreting gas takes place (Fig. 3, Section 4.1). If rotating cooling flows are indeed a requirement for forming thin discs, then we expect thin discs mainly in relatively massive star-forming galaxies in which the CGM has virialized or is composed of subsonic gas, and at low redshift where cold streams are not expected to dominate the accretion. These trends are qualitatively consistent with observations that shows that thin-disc morphologies are prevalent mainly in high-mass and low-redshift star-forming galaxies (Kassin et al. 2012a; Simons et al. 2017).

ACKNOWLEDGEMENTS

ZH was supported by a Gary A. McCue postdoctoral fellowship at UC Irvine. JS was supported by the Israel Science Foundation (grant no. 2584/21) and by the German Science Foundation via DIP grant STE 1869/2-1 GE 625/17-1. JSB was supported by NSF grant AST-1910346. ABG was supported by an NSF-GRFP under grant DGE-1842165 and was additionally supported by NSF grants DGE-0948017 and DGE-145000. SY was supported by NSF grant AST-1910346. CAFG was supported by NSF through grants AST-1715216, AST-2108230, and CAREER award AST-1652522; by NASA through grant 17-ATP17-0067; by STScI through grant *HST*-AR-16124.001-A; and by the Research Corporation for Science Advancement through a Cottrell Scholar Award. DBF is supported by the Simons Foundation through the Flatiron Institute. DAA was supported in part by NSF grants AST-2009687 and AST-2108944 and by the Flatiron Institute, which is supported by the Simons Foundation. EQ was supported in part by a Simons Investigator grant from the Simons Foundation and NSF grant 2107872. AW received support from: NSF grants CAREER 2045928 and 2107772; NASA ATP grant 80NSSC20K0513; *HST* grants AR-15809 and GO-15902 from STScI; a Scialog Award from the Heising-Simons Foundation; and a Hellman Fellowship. MBK acknowledges support from NSF CAREER award AST-1752913, NSF grants AST-1910346 and AST-2108962, NASA grant NNX17AG29G, and *HST*-AR-15006, *HST*-AR-15809, *HST*-GO-15658, *HST*-GO-15901, *HST*-GO-15902, *HST*-AR-16159, and *HST*-GO-16226 from the Space Telescope Science Institute, which is operated by AURA, Inc., under NASA contract NAS5-26555. JM gratefully acknowledges sabbatical leave support from Pomona College and the Harry and Grace Steele Foundation. RF acknowledges financial support from the Swiss National Science Foundation (grant no. PP00P2_194814 and 200021_188552). TKC is supported by Science and Technology Facilities Council (STFC) astronomy consolidated grant ST/P000541/1 and ST/T000244/1. CT and DK were supported by NSF grants AST-1715101 and AST-2108314. Numerical calculations were performed on the Quest computing cluster at Northwestern University, the Wheeler computing cluster at Caltech, XSEDE allocations TG-AST130039, TG-AST120025, TG-AST140064, and TG-AST140023, Blue Waters PRAC allocation NSF.1713353, NASA HEC allocation SMD16-7592, and allocations AST21010 and AST20016 supported by the NSF and TACC. This research benefited from the Halo21 KITP workshop, which was supported in part by the National Science Foundation under grant no. NSF PHY-1748958.

This research used the PYTHON programming language and the following modules: FIREFLY (Geller & Gurvich 2018), NUMPY (Harris et al. 2020), MATPLOTLIB (Hunter 2007), PYTEST (Krekel et al.

2004), JUG (Coelho 2017), H5PY (Collette 2013), SCIPY (Virtanen et al. 2020), PANDAS (McKinney 2010; Reback et al. 2020), PALETTABLE (https://github.com/jiffyclub/palettable), and NUMBA (Lam, Pitrou & Seibert 2015).

DATA AVAILABILITY

The data underlying this article will be shared on reasonable request to the corresponding author (ZH). The simulation initial conditions, snapshot files, and visualization can be found in https://fire.northwestern.edu/data/. A public version of the GIZMO simulation code is available http://www.tapir.caltech.edu/phopkins/Site/GIZMO.html.

REFERENCES

Anglés-Alcázar D., Faucher-Giguère C.-A., Kereš D., Hopkins P. F., Quataert E., Murray N., 2017, MNRAS, 470, 4698
Armillotta L., Fraternali F., Marinacci F., 2016, MNRAS, 462, 4157
Balbus S. A., 1988, ApJ, 328, 395
Balbus S. A., Soker N., 1989, ApJ, 341, 611
Barnes J., Efstathiou G., 1987, ApJ, 319, 575
Behroozi P. S., Wechsler R. H., Conroy C., 2013, ApJ, 770, 57
Benincasa S. M. et al., 2020, MNRAS, 497, 3993
Bernardi M., Shankar F., Hyde J. B., Mei S., Marulli F., Sheth R. K., 2010, MNRAS, 404, 2087
Bertschinger E., 1989, ApJ, 340, 666
Bigiel F., Leroy A., Walter F., Brinks E., de Blok W. J. G., Madore B., Thornley M. D., 2008, AJ, 136, 2846
Birnboim Y., Dekel A., 2003, MNRAS, 345, 349
Bizyaev D., Makarov D. I., Reshetnikov V. P., Mosenkov A. V., Kautsch S. J., Antipova A. V., 2021, preprint (arXiv:2105.11855)
Bluck A. F. L., Mendel J. T., Ellison S. L., Moreno J., Simard L., Patton D. R., Starkenburg E., 2014, MNRAS, 441, 599
Bregman J. N., Anderson M. E., Miller M. J., Hodges-Kluck E., Dai X., Li J.-T., Li Y., Qu Z., 2018, ApJ, 862, 3
Brook C. B. et al., 2011, MNRAS, 415, 1051
Bullock J. S., Dekel A., Kolatt T. S., Kravtsov A. V., Klypin A. A., Porciani C., Primack J. R., 2001, ApJ, 555, 240
Chan T. K., Kereš D., Wetzel A., Hopkins P. F., Faucher-Giguère C.-A., El-Badry K., Garrison-Kimmel S., Boylan-Kolchin M., 2018, MNRAS, 478, 906
Chan T. K., Kereš D., Hopkins P. F., Quataert E., Su K.-Y., Hayward C. C., Faucher-Giguère C.-A., 2019, MNRAS, 488, 3716
Chan T. K., Keres D., Gurvich A. B., Hopkins P., Trapp C., Ji S., Faucher-Giguere C.-A., 2021, preprint (arXiv:2110.06231)
Coelho L. P., 2017, J. Open Res. Softw., 5, 30
Collette A., 2013, Python and HDF5. O'Reilly, Sebastopol, California
Cowie L. L., Fabian A. C., Nulsen P. E. J., 1980, MNRAS, 191, 399
Danovich M., Dekel A., Hahn O., Teyssier R., 2012, MNRAS, 422, 1732
Danovich M., Dekel A., Hahn O., Ceverino D., Primack J., 2015, MNRAS, 449, 2087
Davies J. J., Crain R. A., Pontzen A., 2021, MNRAS, 501, 236
DeFelippis D., Genel S., Bryan G. L., Fall S. M., 2017, ApJ, 841, 16
DeFelippis D., Genel S., Bryan G. L., Nelson D., Pillepich A., Hernquist L., 2020, ApJ, 895, 17
Debattista V. P., Gonzalez O. A., Sanderson R. E., El-Badry K., Garrison-Kimmel S., Wetzel A., Faucher-Giguère C.-A., Hopkins P. F., 2019, MNRAS, 485, 5073
Dekel A., Birnboim Y., 2006, MNRAS, 368, 2
Dekel A. et al., 2009, Nature, 457, 451
Dekel A., Lapiner S., Dubois Y., 2019, preprint (arXiv:1904.08431)
El-Badry K. et al., 2018a, MNRAS, 473, 1930
El-Badry K. et al., 2018b, MNRAS, 477, 1536
Esmerian C. J., Kravtsov A. V., Hafen Z., Faucher-Giguère C.-A., Quataert E., Stern J., Kereš D., Wetzel A., 2021, MNRAS, 505, 1841
Fabian A. C., Nulsen P. E. J., Canizares C. R., 1984, Nature, 310, 733
Faerman Y., Sternberg A., McKee C. F., 2017, ApJ, 835, 52
Faerman Y., Sternberg A., McKee C. F., 2020, ApJ, 893, 82
Fall S. M., Efstathiou G., 1980, MNRAS, 193, 189
Fall S. M., Rees M. J., 1985, ApJ, 298, 18
Faucher-Giguère C., Lidz A., Zaldarriaga M., Hernquist L., 2009, ApJ, 703, 1416
Faucher-Giguère C. A., Kereš D., Ma C. P., 2011, MNRAS, 417, 2982
Faucher-Giguère C.-A., Quataert E., Hopkins P. F., 2013, MNRAS, 433, 1970
Faucher-Giguère C.-A., Hopkins P. F., Kere D., Muratov A. L., Quataert E., Murray N., 2015, MNRAS, 449, 987
Faucher-Giguère C.-A., Feldmann R., Quataert E., Kereš D., Hopkins P. F., Murray N., 2016, MNRAS, 461, L32
Fielding D., Quataert E., McCourt M., Thompson T. A., 2017, MNRAS, 466, 3810
Fielding D. B., Ostriker E. C., Bryan G. L., Jermyn A. S., 2020, ApJ, 894, L24
Garrison-Kimmel S. et al., 2017, MNRAS, 471, 1709
Garrison-Kimmel S. et al., 2018b, MNRAS, 481, 4133
Garrison-Kimmel S. et al., 2018a, MNRAS, 481, 4133
Garrison-Kimmel S. et al., 2019, MNRAS, 487, 1380
Geller A. M., Gurvich A., 2018, Astrophysics Source Code Library, record ascl:1810.021
Genel S., Fall S. M., Hernquist L., Vogelsberger M., Snyder G. F., Rodriguez-Gomez V., Sijacki D., Springel V., 2015, ApJ, 804, L40
Gronke M., Oh S. P., 2020, MNRAS, 494, L27
Guszejnov D., Grudić M. Y., Offner S. S. R., Boylan-Kolchin M., Faucher-Giguère C.-A., Wetzel A., Benincasa S. M., Loebman S., 2020, MNRAS, 492, 488
Hafen Z. et al., 2019, MNRAS, 488, 1248
Hafen Z. et al., 2020, MNRAS, 494, 3581
Harris C. R. et al., 2020, Nature, 585, 357
Heckman T. M., Thompson T. A., 2019, preprint (arXiv:1701.09062)
Hodges-Kluck E. J., Miller M. J., Bregman J. N., 2016, ApJ, 822, 21
Hopkins P. F., 2015, MNRAS, 450, 53
Hopkins P. F., 2017, MNRAS, 466, 3387
Hopkins P. F., Keres D., Onorbe J., Faucher-Giguere C.-A., Quataert E., Murray N., Bullock J. S., 2014, MNRAS, 445, 581
Hopkins P. F. et al., 2018, MNRAS, 480, 800
Hopkins P. F. et al., 2020, MNRAS, 492, 3465
Hopkins P. F., Chan T. K., Squire J., Quataert E., Ji S., Kereš D., Faucher-Giguère C.-A., 2021a, MNRAS, 501, 3663
Hopkins P. F., Chan T. K., Ji S., Hummels C. B., Kereš D., Quataert E., Faucher-Giguère C.-A., 2021b, MNRAS, 501, 3640
Hopkins P. F., Squire J., Chan T. K., Quataert E., Ji S., Keres D., Faucher-Giguere C.-A., 2021c, MNRAS, 501, 4184
Hunter J. D., 2007, Comput Sci Eng., 9, 90
Huscher E., Oppenheimer B. D., Lonardi A., Crain R. A., Richings A. J., Schaye J., 2021, MNRAS, 500, 1476
Ji S. et al., 2020, MNRAS, 496, 4221
Joung M. R., Putman M. E., Bryan G. L., Fernández X., Peek J. E. G., 2012, ApJ, 759, 137
Kassin S. A., de Jong R. S., Weiner B. J., 2006, ApJ, 643, 804
Kassin S. A., Devriendt J., Fall S. M., de Jong R. S., Allgood B., Primack J. R., 2012a, MNRAS, 424, 502
Kassin S. A. et al., 2012b, ApJ, 758, 106
Kelly A. J., Jenkins A., Deason A., Fattahi A., Grand R. J. J., Pakmor R., Springel V., Frenk C. S., 2021, MNRAS, 514, 3113
Kereš D., Hernquist L., 2009, ApJ, 700, L1
Kereš D., Katz N., Weinberg D. H., Davé R., 2005, MNRAS, 363, 2
Kereš D., Katz N., Fardal M., Davé R., Weinberg D. H., 2009a, MNRAS, 395, 160
Kereš D., Katz N., Davé R., Fardal M., Weinberg D. H., 2009b, MNRAS, 396, 2332
Kranz T., Slyz A., Rix H.-W., 2003, ApJ, 586, 143
Kregel M., Van Der Kruit P. C., De Grijs R., 2002, MNRAS, 334, 646
Krekel H., Oliveira B., Pfannschmidt R., Bruynooghe F., Laugher B., Bruhin F., 2004, pytest 3.4, Last access date: May 1, 2022, https://github.com/pytest-dev/pytest
Krumholz M. R., Burkhart B., Forbes J. C., Crocker R. M., 2018, MNRAS, 477, 2716

Lam S. K., Pitrou A., Seibert S., 2015, in Hal F., ed., Proceedings of the Second Workshop on the LLVM Compiler Infrastructure in HPC - LLVM '15. Association for Computing Machinery, New York, NY, United States, p. 1
Li Y., Bregman J., 2017, ApJ, 849, 105
Li J.-T., Crain R. A., Wang Q. D., 2014, MNRAS, 440, 859
Li J.-T., Bregman J. N., Wang Q. D., Crain R. A., Anderson M. E., 2018, ApJ, 855, L24
Lian J., Thomas D., Maraston C., Goddard D., Comparat J., Gonzalez-Perez V., Ventura P., 2018, MNRAS, 474, 1143
Ma X., Hopkins P. F., Wetzel A. R., Kirby E. N., Anglés-Alcázar D., Faucher-Giguère C.-A., Kereš D., Quataert E., 2017, MNRAS, 467, 2430
Maller A. H., Bullock J. S., 2004, MNRAS, 355, 694
Mandelker N., Padnos D., Dekel A., Birnboim Y., Burkert A., Krumholz M. R., Steinberg E., 2016, MNRAS, 463, 3921
Mandelker N., van Dokkum P. G., Brodie J. P., van den Bosch F. C., Ceverino D., 2018, ApJ, 861, 148
Mandelker N., Nagai D., Aung H., Dekel A., Padnos D., Birnboim Y., 2019, MNRAS, 484, 1100
Mandelker N., Nagai D., Aung H., Dekel A., Birnboim Y., van den Bosch F. C., 2020, MNRAS, 494, 2641
Mandelker N., van den Bosch F. C., Springel V., van de Voort F., Burchett J. N., Butsky I. S., Nagai D., Oh S. P., 2021, ApJ, 923, 115
Martin D. C. et al., 2019, preprint (arXiv:1904.11465)
Mathews W. G., Bregman J. N., 1978, ApJ, 224, 308
Mayor M., Vigroux L., 1981, A&A, 98, 1
McCourt M., Sharma P., Quataert E., Parrish I. J., 2012, MNRAS, 419, 3319
McCourt M., Oh S. P., O'Leary R. M., Madigan A.-M., 2018, MNRAS, 473, 5407
McDonald M., Gaspari M., McNamara B. R., Tremblay G. R., 2018, ApJ, 858, 45
McKinney W., 2010, in Python in Science Conference, Austin, Texas, p. 56
McNamara B. R., Nulsen P. E. J., 2007, ARA&A, 45, 117
Mo H. J., Mao S., White S. D. M., 1998, MNRAS, 295, 319
Moffett A. J. et al., 2016, MNRAS, 457, 1308
Murante G., Calabrese M., De Lucia G., Monaco P., Borgani S., Dolag K., 2012, ApJ, 749, L34
Muratov A. L., Kereš D., Faucher-Giguère C.-A., Hopkins P. F., Quataert E., Murray N., 2015, MNRAS, 454, 2691
Muratov A. L. et al., 2017, MNRAS, 468, 4170
Nelson D., Vogelsberger M., Genel S., Sijacki D., Kereš D., Springel V., Hernquist L., 2013, MNRAS, 429, 3353
Nelson D., Genel S., Pillepich A., Vogelsberger M., Springel V., Hernquist L., 2016, MNRAS, 460, 2881
Oppenheimer B. D., 2018, MNRAS, 480, 2963
Pandya V. et al., 2021, MNRAS, 508, 2979
Peebles P. J. E., 1969, ApJ, 155, 393
Peebles P. J. E., 2020, MNRAS, 498, 4386
Pezzulli G., Fraternali F., 2016, MNRAS, 455, 2308
Pezzulli G., Fraternali F., Binney J., 2017, MNRAS, 467, 311
Planck Collaboration, 2018, A&A, 641, 67
Quataert E., Thompson T. A., Jiang Y.-F., 2021a, MNRAS, 510, 1184
Quataert E., Jiang Y.-F., Thompson T. A., 2021b, MNRAS, 510, 920
Reback J. et al., 2020, Pandas-Dev/Pandas: Pandas 1.0.3, Zenodo
Rohr E. et al., 2021, MNRAS, 510, 3967
Sales L. V., Navarro J. F., Theuns T., Schaye J., White S. D. M., Frenk C. S., Crain R. A., Dalla Vecchia C., 2012, MNRAS, 423, 1544
Samuel J. et al., 2020, MNRAS, 491, 1471
Sanderson R. E. et al., 2020, ApJS, 246, 6
Sharma P., Mccourt M., Quataert E., Parrish I. J., 2012, MNRAS, 420, 3174
Simons R. C., Kassin S. A., Weiner B. J., Heckman T. M., Lee J. C., Lotz J. M., Peth M., Tchernyshyov K., 2015, MNRAS, 452, 986
Simons R. C. et al., 2017, ApJ, 843, 46
Sormani M. C., Sobacchi E., Pezzulli G., Binney J., Klessen R. S., 2018, MNRAS, 481, 3370
Stern J., Fielding D., Faucher-Giguère C.-A., Quataert E., 2019, MNRAS, 488, 2549
Stern J., Fielding D., Faucher-Giguère C.-A., Quataert E., 2020, MNRAS, 492, 6042
Stern J. et al., 2021a, MNRAS, 507, 2869
Stern J. et al., 2021b, ApJ, 911, 88
Stevens A. R. H., Lagos C. D. P., Contreras S., Croton D. J., Padilla N. D., Schaller M., Schaye J., Theuns T., 2017, MNRAS, 467, 2066
Stewart K. R., Kaufmann T., Bullock J. S., Barton E. J., Maller A. H., Diemand J., Wadsley J., 2011, ApJ, 738, 39
Stewart K. R., Brooks A. M., Bullock J. S., Maller A. H., Diemand J., Wadsley J., Moustakas L. A., 2013, ApJ, 769, 74
Stewart K. R. et al., 2017, ApJ, 843, 47
Thompson T. A., Quataert E., Murray N., 2005, ApJ, 630, 167
Trapp C. et al., 2021, MNRAS, 509, 4149
Übler H., Naab T., Oser L., Aumer M., Sales L. V., White S. D. M., 2014, MNRAS, 443, 2092
Van de Voort F., Schaye J., 2012, MNRAS, 423, 2991
Van de Voort F., Schaye J., Booth C. M., Dalla Vecchia C., 2011, MNRAS, 415, 2782
van de Voort F., Schaye J., Booth C. M., Haas M. R., Dalla Vecchia C., 2011, MNRAS, 414, 2458
van der Wel A. et al., 2014, ApJ, 792, L6
Virtanen P. et al., 2020, Nature Methods, 17, 261
Voit G. M., 2021, ApJ, 908, L16
Voit G. M., Donahue M., O'Shea B. W., Bryan G. L., Sun M., Werner N., 2015, ApJ, 803, L21
Voit G. M., Meece G., Li Y., O'Shea B. W., Bryan G. L., Donahue M., 2017, ApJ, 845, 80
Wellons S. et al., 2022, preprint (arXiv:2203.06201)
Wetzel A. R., Hopkins P. F., Kim J.-h., Faucher-Giguère C.-A., Kereš D., Quataert E., 2016, ApJ, 827, L23
Wheeler C. et al., 2016, MNRAS, 465, 2420
White S. D. M., Frenk C. S., 1991, ApJ, 379, 52
White S. D. M., Rees M. J., 1978, MNRAS, 183, 341
Yu S. et al., 2021, MNRAS, 505, 889

SUPPORTING INFORMATION

Supplementary data are available at *MNRAS* online.

Hot_Accretion_in_FIRE_AppendixC.pdf
Hot_Accretion_in_FIRE_AppendixD.pdf

Please note: Oxford University Press is not responsible for the content or functionality of any supporting materials supplied by the authors. Any queries (other than missing material) should be directed to the corresponding author for the article.

APPENDIX A: OBSERVATIONALLY MOTIVATED THIN-DISC FRACTION

Fig. A1 shows the relationship between the fraction of stars with $j_z/j_c(E) > 0.8$ at $z = 0$ ($f_{\rm thin\,disk,\,recent}$) and the same fraction of stars weighted by their Sloan r band luminosity-weighted. The figure shows that $f_{\rm thin\,disk,\,recent}$, the thin-disc metric used throughout our analysis, is closely related to the observationally motivated luminosity-weighted thin-disc fraction.

APPENDIX B: SAMPLE VALIDATION

Our main sample of tracked particles for each simulation (Section 2.2) selects particles which accrete from the CGM in the last Gyr prior to $z = 0$. In this appendix, we check the extent to which our sample is representative of all gas that fuels star formation at $z \sim 0$, and the extent to which our sample is representative of all circumgalactic gas. We use the simulation `m12i` as a test case.

Fig. B1 shows the age of the universe at which particles in our main sample accrete on to the main galaxy, compared to the accretion time for all gas which forms stars in the last Gyr. To calculate $t_{\rm acc}$ for all recently formed stars, we track the history of 10^5 randomly selected star particles that formed within the last Gyr, and set $t_{\rm acc}$ to the time of the last accretion event. The $t_{\rm acc}$ distributions for the main sample and the sample probing all recently formed stars largely overlap, indicating our selection method is a representative of star-forming gas in the last Gyr of the simulation.

Fig. B2 compares the properties of all gas in the CGM with the subset of gas which accretes on to the galaxy, where the latter corresponds to the main sample of tracked particles. The top panel shows that most of the accreted gas originates from the inner CGM, likely since cooling times in the hot phase are shorter at small radii. The distributions of specific angular momentum (second panel) and angular momentum alignment (third panel) are similar between the accreted gas and general CGM gas. The bottom panel shows that the median temperature of accreted gas and all CGM gas are similar at $r < 50$ kpc, at which most of the accretion originates, with a tail extending to lower temperatures in the accreted gas. At larger radii, the accreted gas is cooler than general CGM gas, suggesting that from these radii accretion is via cooling of clumps rather than via inflow of the hot medium. Similar results are found in Hafen et al. (2020).

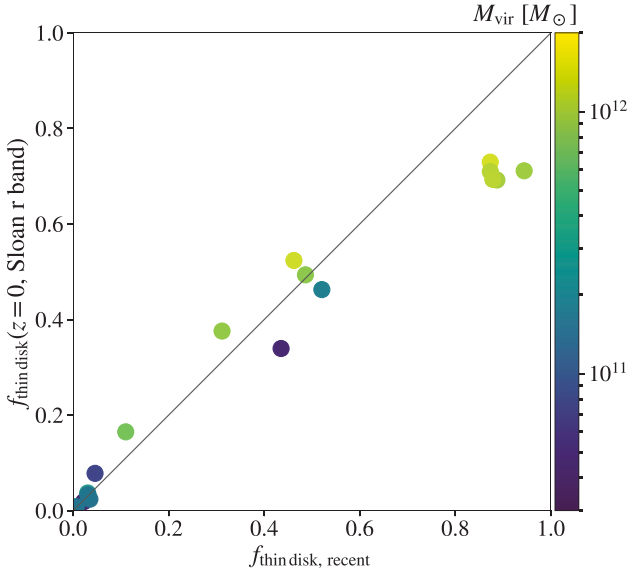

Figure A1. Fraction of recent stars in a thin disc versus Sloan-r-band-weighted thin-disc fraction, in our FIRE sample. The value of $f_{\rm thin\,disk,\,recent}$ closely tracks the observationally motivated luminosity-weighted thin-disc fraction.

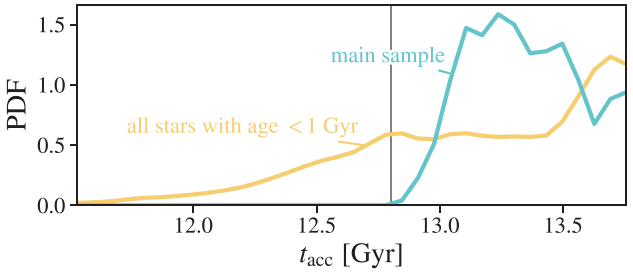

Figure B1. Accretion time distribution for all accreting gas in the last Gyr (green, corresponding to the sample analysed in the main text), compared to accretion time for all gas which forms stars in the last Gyr (yellow), in the `m12i` simulation. Of stars born in the last Gyr, > 70 per cent (> 98 per cent) are formed from gas accreted within the last 1 Gyr (2 Gyr), indicating that the main sample is a representative of all gas which formed recent stars.

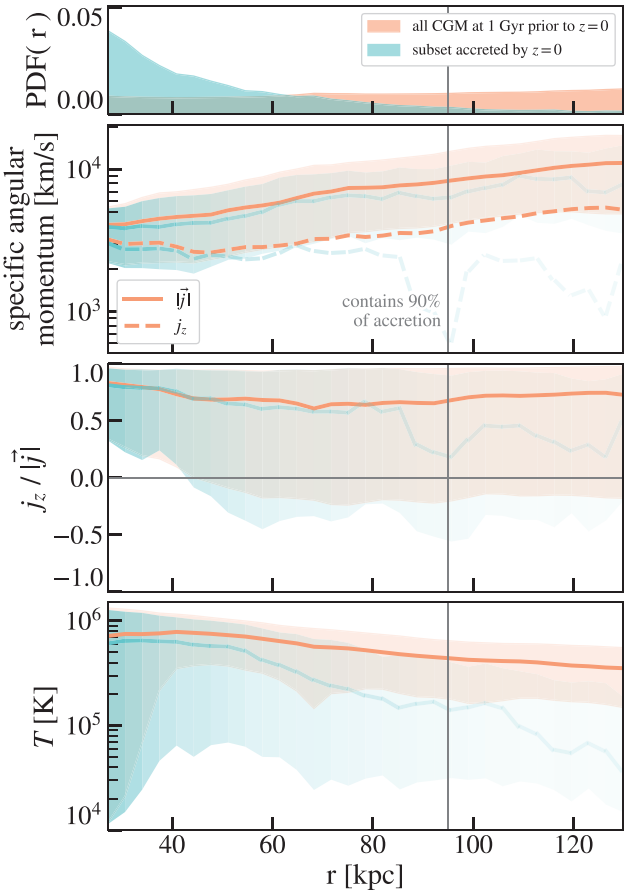

Figure B2. **Top-most panel:** radial distribution of gas in the CGM of `m12i` at 1 Gyr prior to $z = 0$, comparing all gas (orange) to the subset accreted on to the galaxy (green, corresponding to the sample analysed in the main text). Accreted gas mainly originates in the inner CGM. **Bottom panels:** from top to bottom, specific angular momentum, angular momentum alignment, and temperature for both samples. Solid line shows the median, while coloured regions cover 16th–84th percentiles. Accreted gas has similar specific angular momentum and alignment as all gas at the same radii, especially at $r <$ 50 kpc that dominates the accretion. The median temperature is also consistent between the two samples at $r < 50$ kpc, though the distribution extends to lower temperatures in the accreted sample.

This paper has been typeset from a TEX/LATEX file prepared by the author.